Joint optimization of geophysical data using multi-objective swarm intelligence

Geophysical Journal International

Geophys. J. Int. (2019) **0,** 1–0 doi: 10.1093/gji/ggz243

GJI Marine geosciences and applied geophysics

Joint optimization of geophysical data using multi-objective swarm intelligence

Francesca Pace,[1] Alberto Godio,[1] Alessandro Santilano[2] and Cesare Comina[3]

[1] *Department of Environment, Land and Infrastructure Engineering (DIATI), Politecnico di Torino, Corso Duca degli Abruzzi 24, 10129, Turin, Italy. E-mails: francesca.pace@polito.it; alberto.godio@polito.it*

[2] *Institute of Geosciences and Earth Resources- National Research Council (IGG-CNR), Via Moruzzi 1, 56124, Pisa, Italy*

[3] *DST, Università degli Studi di Torino, Via Valperga Caluso 35, 10125,Turin, Italy*

Accepted 2019 May 22. Received 2019 April 29; in original form 2018 December 21

SUMMARY

The joint inversion of multiple data sets encompasses the advantages of different geophysical methods but may yield to conflicting solutions. Global search methods have been recently developed to address the issue of local minima found by derivative-based methods, to analyse the data compatibility and to find the set of trade-off solutions, since they are not unique. In this paper, we examine two evolutionary algorithms to solve the joint inversion of electrical and electromagnetic data. These nature-inspired metaheuristics also adopt the principle of Pareto optimality in order to identify the result among the feasible solutions and then infer the data compatibility. Since the joint inversion is characterized by more than one objective, we implemented the algorithm multi-objective particle swarm optimization (MOPSO) to jointly interpret time-domain electromagnetic data and vertical electrical sounding. We first tested MOPSO on a synthetic model. The performance of MOPSO was directly compared with that of a multi-objective genetic algorithm, the non-dominated sorting genetic algorithm (NSGA-III), which has often been adopted in geophysics. The adoption of MOPSO and NSGA-III enabled avoiding both simplification into a single-objective problem and the use of a weighting factor between the objectives. We tested the two methods on real data sets collected in the northwest of Italy. The results obtained from MOPSO and NSGA-III were highly comparable to each other and largely consistent with literature findings. The MOPSO performed a rigorous selection of the best trade-off solutions and its convergence was faster than NSGA-III. The analysis of the Pareto Front reported data incompatibility, which is very common for real data due to different resolutions, sensitivities and depth of investigations. Notwithstanding this, the multi-objective optimizers provided a complementary interpretation of the data, ensuring significant advantages with respect to the separate optimizations we carried out using the single-objective particle swarm optimization algorithm.

Key words: Non-linear electromagnetics; Joint inversion; Numerical solutions; Statistical methods.

1 INTRODUCTION

The joint inversion of multiple data sets can significantly improve their modelling by overcoming the intrinsic limitations of each geophysical method. The advantages in combining different geophysical measurements using a unique inversion scheme have been clear since the first introduction of joint inversion methods (Vozoff & Jupp 1975; Yang & Tong 1988). Joint inversion has been extensively applied to electrical and electromagnetic data to interpret one physical property, that of electrical conductivity. However, as with single inversion, joint inversion is still affected by non-uniqueness, nonlinearity and ill-posedness, meaning that many different models can fit the data within a certain misfit range (Tarantola 2005).

In the last decade, many derivative-based methods have been proposed for the joint inversion of different data sets. These methods have proved to successfully image the properties of the layered subsurface, thus outperforming the separate inversions and the correspondent ambiguities (Hering *et al.* 1995; Gallardo & Meju 2003; Musil *et al.* 2003; Moorkamp *et al.* 2011). A main issue with joint inversion is data compatibility since real-world data are acquired using different methods and usually present different resolutions, sensitivities, depth of investigations and/or error levels. Data incompatibility can hence lead to either a variety of final results or

conflicting models. These are commonly avoided using a weighting factor between the objective functions that rule the inversion (Candansayar & Tezkan 2008; Commer & Newman 2009; Meqbel & Ritter 2015). However, even when using appropriate weighting factors, the choice of the proper one is still critical and may not resolve the conflict (Akca *et al.* 2014). Moreover, the search for a single best solution for a joint-inversion problem can still produce biased results. Therefore, the main drawbacks of the derivative-based joint inversion are (1) the simplification of a multi-objective (MO) problem (joint inversion) into a succession of single-objective optimization problems with weighted objective functions and (2) the strong influence of the starting model on the final result, which is typical of the deterministic inversion techniques.

MO evolutionary algorithms (MOEAs) have recently been proposed for the joint inversion of multiple data sets because they deploy an MO optimizer (MOO) to solve the problem, without transforming it into a series of single-objective optimizations. This approach avoids the adoption of user-dependent weighting factors. MOEAs rate the solution quality using the concept of Pareto optimality, first introduced by Edgeworth (1881) and Pareto (1896). A solution is considered Pareto optimal if there is not another feasible solution that improves one objective without deteriorating the other objective. The whole set of solutions that fulfils this criterion is called the Pareto-optimal set. MOEAs are attracting widespread interest since the objective function is a unique vector of as many components as the different data sets to be optimized, without any need to rank them. The most widely used EAs are the genetic algorithm (GA) and the particle swarm optimization (PSO) algorithm (Kennedy & Eberhart 2001; Engelbrecht 2007). In geophysics, the PSO algorithm has been accurately investigated to solve the inverse problem involving vertical electrical sounding (VES; Fernandez Martinez *et al.* 2010), direct current (DC) method (Shaw & Srivastava 2007), audio-magnetotelluric (AMT) and MT data (Pace *et al.* 2017; Godio & Santilano 2018; Pace *et al.* 2019), MT and time-domain electromagnetic (TDEM) data (Santilano *et al.* 2018). Due to the positive outcomes of PSO applied to single-objective problems, it has been proposed to tackle MO problems. Coello Coello *et al.* (2004) showed highly competitive results of MO particle swarm optimization (MOPSO) applied to benchmark test functions. Unfortunately, few studies have so far dealt with MOPSO applied to geophysics. One of the first works that adopted PSO for the joint inversion of synthetic data (GPR and *P*-wave seismic traveltimes) was Tronicke *et al.* (2011), but it actually simplified the problem into a single-objective one. Similarly, Paasche & Tronicke (2014) developed a hybrid approach on radar and *P*-wave traveltimes. Cheng *et al.* (2015) then applied PSO to a whole forward process synchronized between transient electromagnetic method (TEM) and DC methods. There is hence little evidence of the potentiality of MOPSO on the geophysical joint inversion. The MO version of GA has instead been more explored; examples include the inversion of Raleigh-wave dispersion curves and reflection traveltimes (Dal Moro & Pipan 2007), surface wave dispersion and horizontal-to-vertical spectral ratio (Dal Moro 2010), AMT and broad-band MT data (Schnaidt *et al.* 2018), magnetic resonance and VES data (Akca *et al.* 2014), seismic and well-log data for reservoir modelling (Emami Niri & Lumley 2015), and receiver functions, surface wave dispersion and MT data (Moorkamp *et al.* 2010). Although these works have adopted the non-dominated sorting GA called NSGA-II (Deb *et al.* 2002), little attention has been paid to the most recent NSGA-III (Deb & Jain 2014).

This work explores the 1-D joint inversion of different geophysical data sets using MOPSO as the MO solver since its potential has not been fully investigated so far. Each data set was composed of integrated TDEM and VES soundings, so we dealt with a bi-objective problem. The adoption of MOEAs avoided both simplification into a single-objective problem and the use of the weighting factor. A preliminary introduction on our method can be found in Pace *et al.* (2018). The novelty of this paper is that our method is first tested on synthetic data and then applied to two real data sets from two different surveys for groundwater prospection in northwest Italy (Piedmont region). Moreover, the performance of MOPSO applied to real data was directly compared with that of a NSGA-III, which is stable and widely adopted in geophysics. The economic concept of Pareto optimality was used to identify the final set of results among the feasible solutions. We present also the advantages of the MOPSO with respect to the separate PSO inversions.

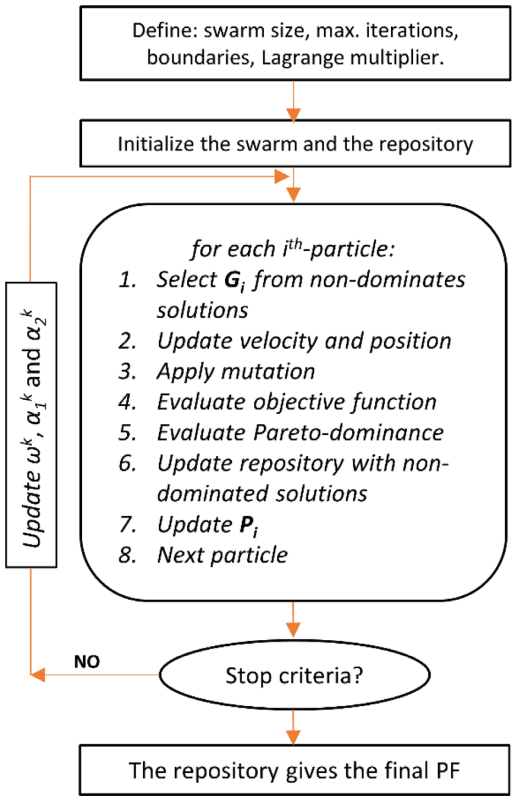

Figure 1. The scheme of the TV-MOPSO algorithm.

2 METHOD

2.1 The objective function and Pareto optimality

The EAs are nature-inspired and population-based metaheuristics that simulate the complex social dynamics of groups of animals to find the optimized solution of a nonlinear problem. The MO version of these algorithms has been developed to solve that problems characterized by more than one objective, as explained in Coello Coello *et al.* (2007). The joint inversion of multiple geophysical data sets is an example of MO problem. The MOEAs adopted in this work are the MO versions of PSO and GA, the MOPSO and NSGA-III algorithms, respectively. Dealing with different geophysical measurements at the same site makes the inversion critical because the resolution, sensitivity and depth of investigation can extremely vary from one method to another. Consequently, the interpretation of the data can yield to conflicting solutions and the components

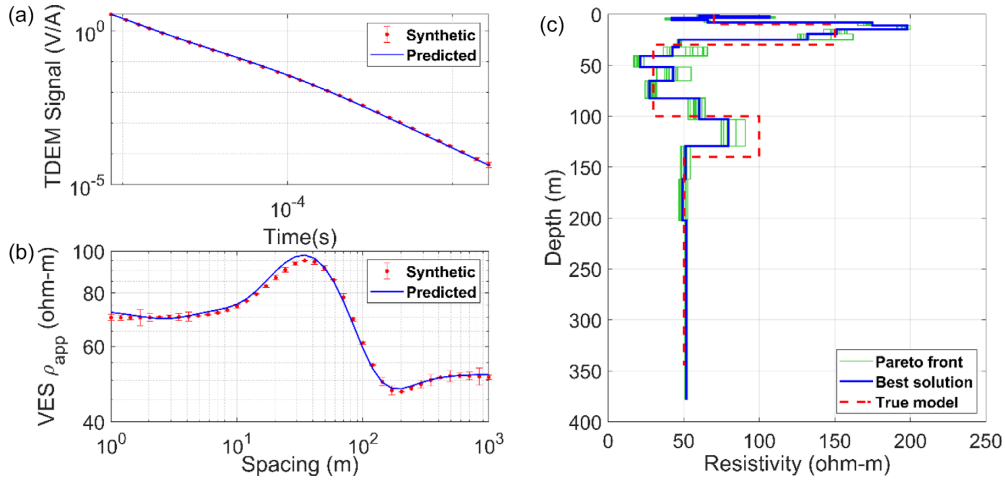

Figure 2. The result of TV-MOPSO applied to the synthetic example: (a) TDEM theoretical signal (the red dots with error bars) and predicted response in the range 0.9×10^{-5}–2×10^{-3} s, (b) VES data cover 1–1000 m of half-spacing, (c) the true model (the red-dashed line), the final resistivity models derived from the *PF* (the green lines) and the best solution highlighted in blue.

of the objective function may not converge. The optimization of different physical parameters may further influence the problem of conflicting solutions.

In this study, we jointly analysed two geophysical methods, TDEM and VES, which deal with the same physical parameter, that is, electrical resistivity. The problem unknown was the *p*-dimensional vector $\boldsymbol{m} = [m_1, \ldots, m_p]$ of electrical resistivity, being *p* the number of layers whose thickness was defined before the optimization. The 1-D profile $\boldsymbol{m}$ is a feasible solution found after the minimization of the objective function:

$$\boldsymbol{f}\ (\boldsymbol{m}) = [f_1(\boldsymbol{m}),\ f_2(\boldsymbol{m})], \tag{1}$$

where the two components of the vector refer to TDEM and VES, respectively. These components were simultaneously minimized in the multidimensional space of the objective function.

Since a variety of solutions is identified at the end of the MO optimization, the choice of the best solution is a critical point. MOEAs select the best set of trade-off solutions using the optimality notion originally proposed by Edgeworth (1881), then generalized by Vilfredo Pareto and today well known as the *Pareto optimality* (Pareto 1896). This principle identifies a range of compromises as feasible solutions, thus avoiding the results being biased by the user-driven weighting approach. This is the mathematical definition of *Pareto dominance*: given two possible solutions $\boldsymbol{m_a}$ and $\boldsymbol{m_b}$, the vector $\boldsymbol{f(m_a)}$ is said to dominate $\boldsymbol{f(m_b)}$ (denoted by $\boldsymbol{f(m_a)} \preccurlyeq \boldsymbol{f(m_b)}$) if and only if $\forall j \in \{1, 2\}, \boldsymbol{f_j(m_a)} \leq \boldsymbol{f_j(m_b)} \barwedge \exists j \in \{1, 2\} : \boldsymbol{f_j(m_a)} < \boldsymbol{f_j(m_b)}$. For us, $j = 1$ refers to the TDEM component and $j = 2$ to the VES component. All the non-dominated solutions form the Pareto-optimal set ($P*$) or non-dominated set. The corresponding objective functions of the non-dominated solutions form the Pareto front (*PF*) in the objective space:

$$PF = \{\boldsymbol{f}\ (\boldsymbol{m}) = (\boldsymbol{f_1}(\boldsymbol{m}), \boldsymbol{f_2}(\boldsymbol{m}))|\boldsymbol{m} \in P^*\}. \tag{2}$$

That is, when $P*$ is projected onto a surface, it is referred to as the *PF*. In our 2-D objective space, the *PF* is graphically depicted as a trade-off surface showing which component of $\boldsymbol{f(m)}$ is mostly minimized. Besides, the *PF* can be analysed to infer the compatibility between the different data sets (Dal Moro & Pipan 2007; Schnaidt *et al.* 2018).

Each *j*th component of the objective function to be minimized was defined as the Euclidean norm of the misfit between observed data and calculated response plus an additional term to regulate the model smoothness:

$$f_j(\boldsymbol{m}) = \left\| \frac{\boldsymbol{\varphi}_o - \boldsymbol{\varphi}_c}{\boldsymbol{\sigma}_\varphi} \right\|_2 + \lambda_j \parallel \log_{10}(\partial \boldsymbol{m})\|_2, \tag{3}$$

where $\varphi_{a,o}$ is the observed TDEM signal if $j = 1$ or the observed apparent resistivity if $j = 2$; $\varphi_{a,c}$ is the calculated response for TDEM signal if $j = 1$ or the calculated apparent resistivity if $j = 2$; the difference in $\|\cdot\|_2$ is normalized by the corresponding errors (σ_φ) on the observed data; λ_j is called the Lagrange-multiplier, or smoothing parameter. The right-hand side of eq. (3) is composed of two terms: the first one assesses the distance of the observed data from the response calculated by the forward modelling; the second term addresses the minimization of the roughness of the model, using the smoothing parameter λ_j on the first derivative of the model $\boldsymbol{m}$. The subscript of λ_j addressed the different level of smoothing required by the specific geophysical method. Even though the Occam's inversion was first introduced for deterministic methods (Constable *et al.* 1987), the 'Occam-like optimization' has been effectively proposed for PSO in Godio & Santilano (2018), Pace *et al.* (2019) and Santilano *et al.* (2018). We here applied the 'Occam-like optimization' in order to search for the smoothest model that fitted the data, that is, a trade-off between the minimum misfit achievable and unnecessary structure (or roughness) in the model. The proper value of λ_j was chosen following the L-curve criterion, which identified the optimal trade-off between the misfit

Table 1. Analysis of the performance of MOPSO on the synthetic example. The rows report the number of iterations run, repository index (*RI*), spacing (*SP*), deviation angle (α) between the ideal and Theil–Sen regression line, total runtime in hours, data misfit (NRMSE) for TDEM and VES and model misfit (NRMSE).

Synthetic data	MOPSO
Iterations	1000
RI (per cent)	7.6
SP	0.0033
α (°)	48.3
Runtime (h)	13
Data NRMSE TDEM	0.0367
Data NRMSE VES	0.0209
Model NRMSE	0.188

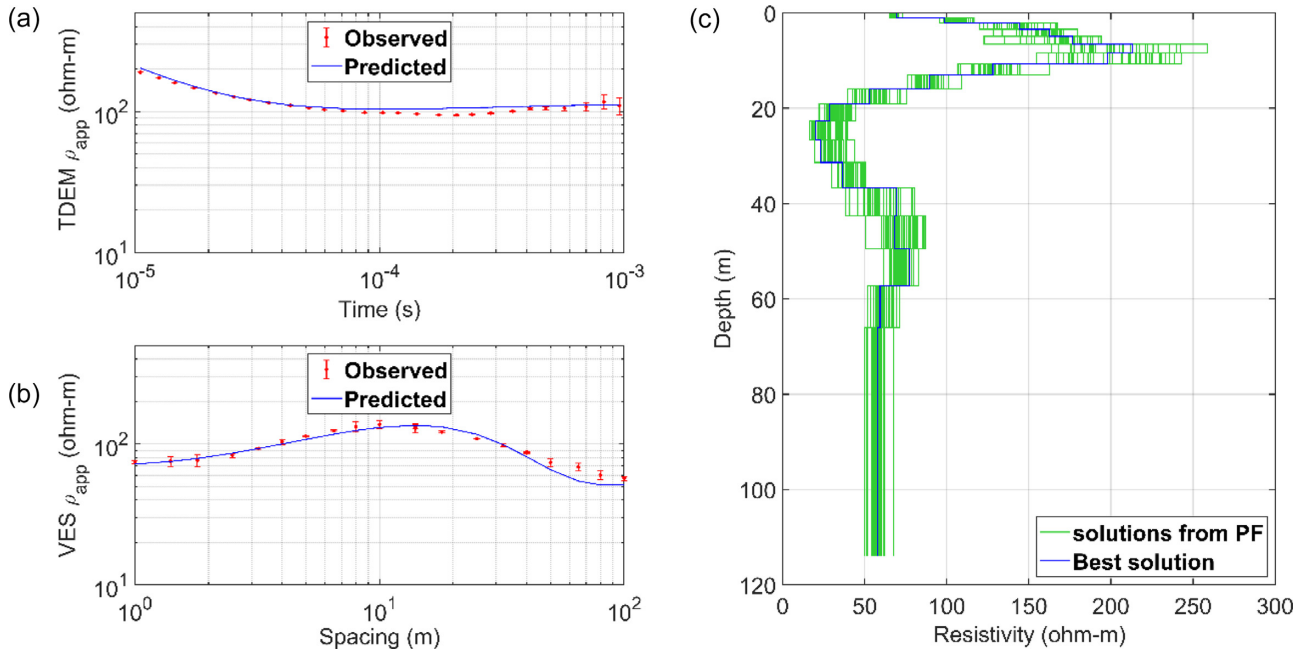

Figure 3. The result of TV-MOPSO applied to the Stupinigi data set: observed data (the red dots with error bars) and predicted apparent resistivity (ρ_{app}) for TDEM (a) and VES (b) data; (c) the final resistivity models derived from the *PF* (the green lines) and the best solution highlighted in blue.

of the data and the roughness of the final model (i.e. the model norm; Farquharson & Oldenburg 2004). It is obvious from eq. (3) that a high value of λ_j results in a smooth model penalizing the misfit, while, on the contrary, a low λ_j yields a minimum data misfit and high resistivity contrasts (roughness) between the layers of the model. The forward modelling used to handle TDEM data was derived from the CR1Dmod algorithm (Ingeman-Nielsen & Baumgartner 2006). The VES forward modelling was adapted from the code VES1dmod in Ekinci & Demirci (2008).

The MO optimization of TDEM and VES data was defined as a problem without equality and inequality constraints. The problem had boundary conditions: the search space of the solutions was bounded between a minimum and maximum value of electrical resistivity. This interval was set as large to enable the exploration of all the feasible solutions.

2.2 The multi-objective particle swarm optimization algorithm

The PSO algorithm is a population-based algorithm inspired by the social behaviour of animals such as flocks of birds or schools of fish. Fundamental theory can be found in Kennedy & Eberhart (1995, 2001) and Engelbrecht (2007). Successful applications of PSO have covered a wide variety of scientific disciplines (Poli 2008 and references therein). We here explain the main differences between single-objective PSO and MOPSO in relation to the geophysical inversion. The particles of the swarm occupied the search space of solutions and represented the possible solutions of joint inversion. After starting from a random distribution, the adaptive behaviour adjusted the particles' positions and ruled their interactions in order to minimize the objective function (eq. 3). This complex behaviour ensured, iteration after iteration, the exploration and exploitation of the search space and, finally, the convergence of the solution (Fernández Martínez *et al.* 2010; Pallero *et al.* 2018). The particles iteratively changed their positions according to

$$\boldsymbol{v}_i^{k+1} = \omega^k\, \boldsymbol{v}_i^k + \alpha_1^k \gamma_1 \left(\boldsymbol{P}_i - \boldsymbol{x}_i^k\right) + \alpha_2^k \gamma_2 \left(\boldsymbol{G}^{\boldsymbol{k}} - \boldsymbol{x}_i^k\right), \tag{4}$$

$$\boldsymbol{x}_i^{k+1} = \boldsymbol{x}_i^k + \boldsymbol{v}_i^{k+1}, \tag{5}$$

where $i = [1,\ldots,N]$; N is the number of particles; k is the iteration number; $\boldsymbol{x}_i^k$ and $\boldsymbol{v}_i^k$ are the current vectors of position and velocity of the ith particle, respectively; ω^k is the inertia weight that linearly decreases from 0.9 (first iteration) to 0.4 (last iteration) in order to tune the momentum remembered from the previous iteration (Shi & Eberhart 1999); $\alpha_1{}^k$ is the cognitive acceleration towards the particle best solution $\boldsymbol{P_i}$, also called 'local best'; $\alpha_2{}^k$ is the social acceleration towards the best global position $\boldsymbol{G}$, also called 'global best'; γ_1 and γ_2 are random numbers, uniformly distributed in [0, 1] to provide stochastic perturbation to the solutions found. While in single-objective PSO the leader $\boldsymbol{G}$ is the unique best particle of the swarm, in MOPSO the set of non-dominated solutions worked as swarm leader. The non-dominated solutions were stored in an archive called *repository.* It was updated at each k iteration with the advantage that a high number of iterations did not directly imply a high number of non-dominated solutions since a new non-dominated solution could dominate (and hence replace) a non-dominated solution of the previous iteration (Coello Coello *et al.* 2004). $\boldsymbol{G}^k$ was hence selected from the repository at each iteration according to a quasi-random criterion based on the most crowded regions of the objective space. Eq. (4) establishes that the particle's velocity resulted from the balance among three terms: the cognitive knowledge $\alpha_1{}^k$, the social attraction $\alpha_2{}^k$ towards the leader and the inertia ω^k, accounting for the past experience. At the first iteration ($k = 0$), the particles were initialized with null velocity ($\boldsymbol{v}_i^0 = 0$) and random positions uniformly distributed in the search space.

Since the first appearance in 2000, several MOPSO variants have been proposed (for a review, see Reyes-Sierra & Coello Coello 2006). We implemented the time-variant (or TV) MOPSO to take

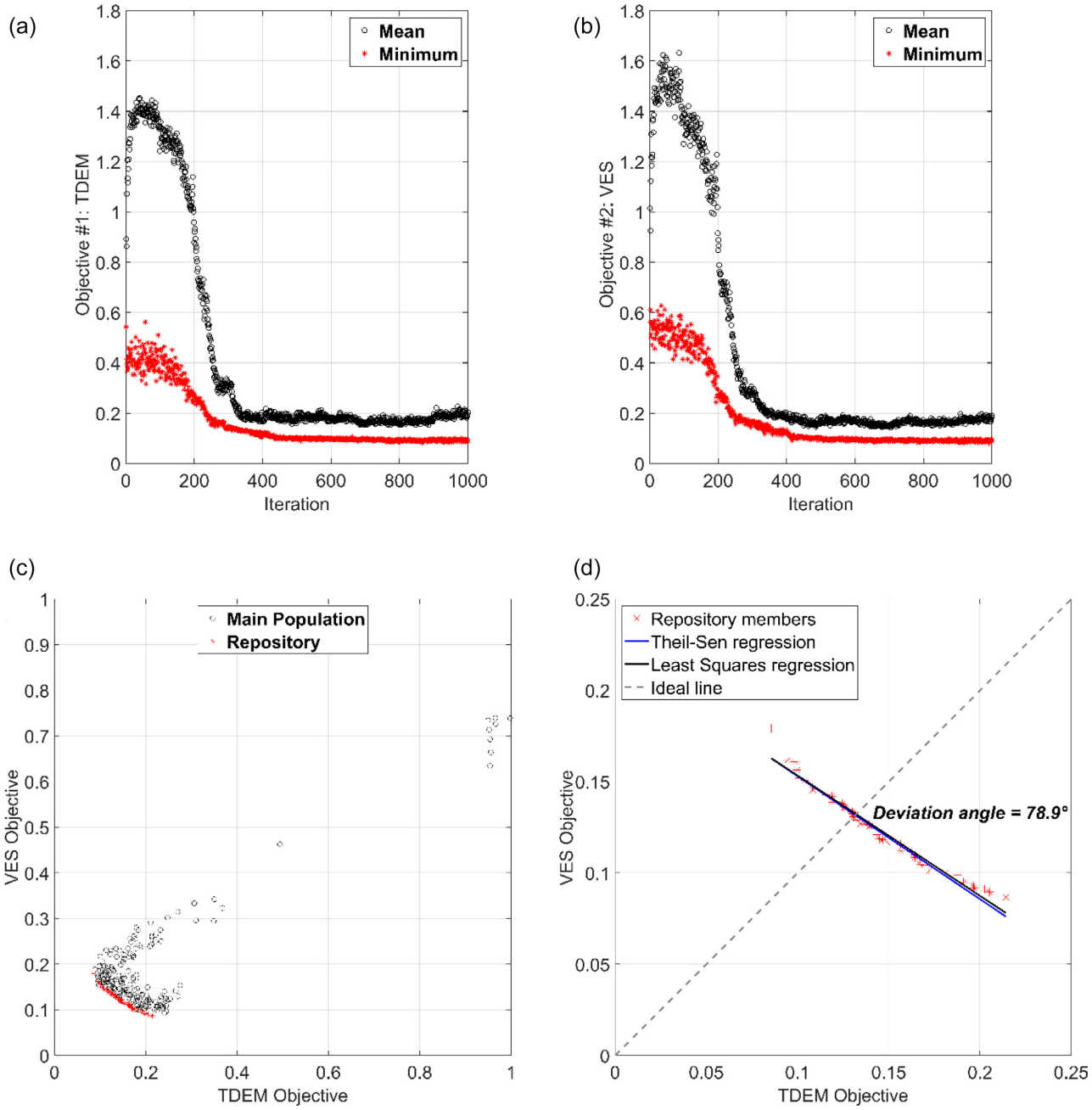

Figure 4. TV-MOPSO applied to the Stupinigi data set: the evolution of the TDEM (a) and VES (b) components of the objective function from the first to the last iteration for the best particle (the red stars) and the remaining ones (the black circles); (c) the 2-D space of the objective function (TDEM and VES components) at the last iteration: the red symbols identify the *PF* and the black circles the objective-function values assumed by the other solutions; (d) the intersection between the ideal line (grey dashed) and the Theil–Sen regression line (blue) or the least-squares regression line (black) identifies the deviation angle α.

advantage of the k-dependent coefficients ω^k, $\alpha_1{}^k$ and $\alpha_2{}^k$ changing at each iteration to provide global exploration of the search space at the beginning of the optimization and local exploitation at the end. In detail, the TV inertia weight was proposed by Shi & Eberhart (1999), while the TV acceleration coefficients by Ratnaweera *et al.* (2004) and Tripathi *et al.* (2007). These works clearly demonstrated that a high $\alpha_1{}^k$ improves the solution diversity, while a high $\alpha_2{}^k$ fosters the convergence towards the global best. Therefore, we set $\alpha_1{}^k$ larger than $\alpha_2{}^k$ at the initial iterations. Then, during the optimization, $\alpha_1{}^k$ linearly decreased and $\alpha_2{}^k$ linearly increased, so that at the end they were reversed. In detail

$$\alpha_1^k = \alpha_1^{\max} - (\alpha_1^{\max} - \alpha_1^{\min}) \left(\frac{k-1}{\max(k)-1} \right), \quad (6)$$

$$\alpha_2^k = \alpha_2^{\min} + (\alpha_2^{\max} - \alpha_2^{\min}) \left(\frac{k-1}{\max(k)-1} \right), \quad (7)$$

where α^k is the acceleration value at iteration k; $\alpha_1{}^{\max}$ and $\alpha_2{}^{\max}$ are the maximum values for the cognitive and social accelerations, respectively; $\alpha_1{}^{\min}$ and $\alpha_2{}^{\min}$ are the minimum values for the cognitive and social accelerations, respectively; and max(k) is the

Table 2. Analysis of the performance of MOPSO and NSGA-III on the data set from Stupinigi. The rows report the number of iterations run, repository index (*RI*), spacing (*SP*), deviation angle (α) between the ideal and Theil–Sen regression line, total runtime in hours and normalized root-mean-square error (NRMSE) for TDEM and VES.

Stupinigi data set	MOPSO	NSGA-III
Iterations	1000	1000
RI (per cent)	21.5	100
SP	0.0041	0.0023
α (°)	78.9	79.2
Runtime (h)	8.9	8.3
NRMSE TDEM	0.1611	0.2728
NRMSE VES	0.0681	0.0645

maximum number of iterations set for the optimization (Engelbrecht 2007 and references therein). Therefore, at the first iteration ($k = 1$), $\alpha_1^{k=1} = \alpha_1^{\max}$ and $\alpha_2^{k=1} = \alpha_2^{\min}$, while, at the last iteration ($k = \max(k)$), $\alpha_1^{k=\max(k)} = \alpha_1^{\min}$ and $\alpha_2^{k=\max(k)} = \alpha_2^{\max}$. Following the stability criteria in Perez & Behdinan (2007) and the sensitivity analysis in Pace *et al.* (2019), we set $\alpha_1^{\max} = \alpha_2^{\max} = 2$ and $\alpha_1^{\min} = \alpha_2^{\min} = 0.5$.

Our TV-MOPSO algorithm included the mutation operator, which is typical of GA and scarcely effective in single-objective PSO. However, many theoretical studies have proposed the introduction of the mutation operator in MOPSO, in order to boost the exploration of the remote regions of the search space and prevent premature convergence to the local *PF* (Coello Coello *et al.* 2004; Tripathi *et al.* 2007). We adopted the mutation operator equal to 0.5, in line with that works. It operated on a wide percentage of particles at the early iterations and then exponentially decreased its influence towards the end. The main advantage of the mutation operator is that it compensates for the loss of diversity throughout the optimization process.

The algorithm ran until a specific number of iterations was achieved, that is, up to 1000 iterations. However, the total number of iterations is problem dependent and its initial and arbitrary choice has proven to be inadequate as the single stopping criterion (Engelbrecht 2007). Few iterations can lead to premature ending before the solution convergence and, on the other hand, too much iterations can result in unnecessary computation. Therefore, we set another stopping criterion: if the objective function did not minimize for 300 consecutive iterations, the run was terminated.

Another fundamental setting of the MOPSO was the number of particles forming the swarm, that is, population size. This setting is dependent on the number of unknowns of the problem, namely, the number of layers the 1-D profile was discretized into. The rule of thumb prescribes the number of particles proportional to about 8–12 times the unknowns (Engelbrecht 2007; Fernández Martínez *et al.* 2010; Pace *et al.* 2019). We discretized the model into 19 layers and set the swarm size equal to about nine times the unknowns, that is, a total of 170 particles. The scheme of the MOPSO algorithm is listed in the flowchart of Fig. 1.

Our algorithm was developed in the Matlab programming environment using the Parallel Computing Toolbox. The general code of TV-MOPSO was adapted from Coello Coello *et al.* (2004) for the geophysical problem. The simulations ran on a 12-core node of the high performance computing (HPC) cluster for academic research at Politecnico di Torino. The CPU model of the single node is 2x Intel Xeon E5–2680 v3 2.50 GHz 12 cores. The sustained performance of the cluster is globally 20.13 TFLOPS.

2.3 The NSGA-III

This section briefly describes the NSGA-III, being our study focused on swarm intelligence. NSGA-III was essentially chosen as basis of comparison for MOPSO since GAs are the most common global optimizers in geophysics. The NSGA-III is a bio-inspired metaheuristic that mimics the inheritance of the highest qualities from parents to children, the natural selection and the biodiversity. The population members represented the possible solutions of joint inversion and were sorted according to the Pareto-dominance *ranking* method. The selection of the non-dominated solutions was performed using the non-domination rank and the so-called *crowding distance* that measured the neighbours surrounding each individual. The diversity was preserved according to the tenet of *fitness sharing* that promoted the solutions in the least populated regions of the search space (Coello Coello *et al.* 2007). These criteria of ranking and selection allowed the Pareto-optimal set to be identified.

Some input arguments of NSGA-III were similar to MOPSO and hence were set following the criteria explained in the previous section. These inputs were the population size, the number of iterations, the boundary conditions and the stopping criteria. The main difference between NSGA-III and MOPSO are the genetic operators known as crossover and mutation, the number of reference points and the absence of the external archive called repository. The crossover percentage was 0.5, meaning that, given any two random parents, half of the population of the new generation, namely the offspring, was subjected to the genetic crossover. The mutation percentage was 0.5 too, so that half of the population was subjected to mutation. In detail, the mutation rate was 0.02, meaning that the 2 per cent of the model represented by each selected individual was forced to mutate. A major novelty of NSGA-III compared to NSGA-II is the adoption of the reference points in order to enhance the diversity among the solutions found. In a two-objective problem, the reference points are placed in the line that in the 2-D objective space intercept the axes in 1. The population members associated with the reference points are emphasized, that is, allowed to evolve in the next generation (elitist selection). It has been proven that the most adequate number of reference points is equal to the population size, so we set it accordingly. This and further details are given in Deb & Jain (2014), which also reports the other differences and advantages with respect to the well-known NSGA-II.

2.4 Solution evaluation

We adopted three metrics as performance measures assessing both the number of non-dominated solutions and the *PF*.

(1)The repository index (*RI*):

$$RI\ (\text{per cent}) = \frac{N_{\text{rep}}}{N_{\text{tot}}}, \tag{8}$$

where N_{rep} is the number of non-dominated solutions (or, in MOPSO, the particles stored in the repository), and N_{tot} is the total number of solutions analysed (i.e. the population size in both MOPSO and NSGA-III). *RI* measured the level of non-dominated solutions at the last iteration.

(2)The spacing (*SP*):

$$SP = \sqrt{\frac{1}{N_{\text{rep}} - 1} \sum_{i=1}^{N_{\text{rep}}} \left(\bar{d} - d_i\right)^2}, \tag{9}$$

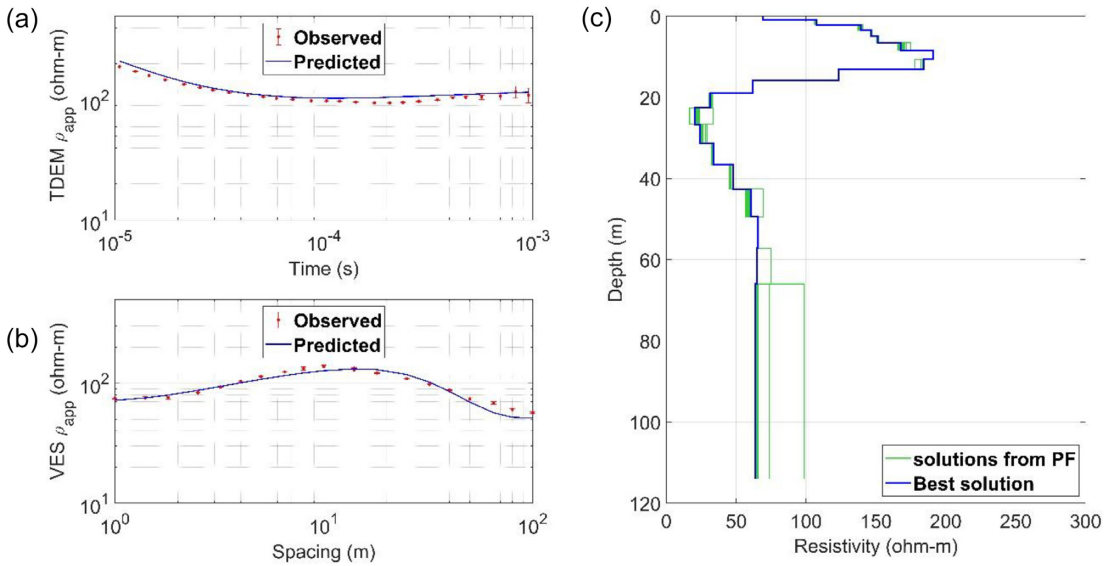

Figure 5. The result of NSGA-III applied to the Stupinigi data set: observed data (the red dots with error bars) and predicted apparent resistivity (ρ_{app}) for TDEM (a) and VES (b) data; c) the final resistivity models derived from the *PF* (the green lines) and the best solution highlighted in blue.

where $d_i = \min_j (|f_1^i(\boldsymbol{m}) - f_1^j(\boldsymbol{m})| + |f_2^i(\boldsymbol{m}) - f_2^j(\boldsymbol{m})|); i, j = 1, \ldots, N_{rep}$, and $\bar{d}$ is the mean of all d_i (Coello Coello *et al.* 2004). This metric effectively measured the distribution of the solutions throughout the *PF* and was 0 in case of uniform distribution (i.e. equidistant spacing) between the beginning and the end of the *PF* curve.

(3)The deviation angle ($\boldsymbol{\alpha}$) between two lines: the bisector of the objective space (with slope 1) and the linear fit of the *PF* calculated using the Theil–Sen estimator (Theil 1950; Sen 1968). The angle α was derived from the tangent:

$$\tan\alpha = \left|\frac{\tilde{m} - 1}{1 + \tilde{m}}\right|, \tag{10}$$

where $\tilde{m}$ is the median of the slopes between all the possible pairs of points of the 2-D *PF* $\{(x_i, y_i)|i = 1, \ldots, N_{rep}\}$:

$$\tilde{m} = \text{median}\left\{m_{i,j} \,|i, j = 1, \ldots, N_{rep}, \; i \neq j, \; i) j\right\}, \tag{11}$$

$$m_{i,j} = \frac{y_j - y_i}{x_j - x_i}. \tag{12}$$

The deviation angle $\boldsymbol{\alpha}$ is an indicator of the data set compatibility because only if the data sets are perfectly compatible, the objective components converge to the same value and the *PF* aligns along the ideal line of slope 1 (Schnaidt *et al.* 2018). Otherwise, conflicting objective components lead to a marked deviation of the Theil–Sen regression line. In detail, the condition $0^\circ < \alpha < 45^\circ$ proves data compatibility and can be easily observed in case of synthetic data sets. If, instead, $45^\circ < \alpha < 90^\circ$ data incompatibility occurs, and the *PF* deviates from the ideal line. Unfortunately, field data sets are commonly affected by incompatibility or partial compatibility due to the specific differences of the geophysical methods. However, the regression line, or simply, the *PF* shape is effective in showing how much one objective component is in contrast with the other one (Dal Moro 2010).

3 MULTI-OBJECTIVE OPTIMIZATION OF SYNTHETIC AND FIELD DATA SETS

The MOPSO was first tested on synthetic data to evaluate the performance of the algorithm. Then, it was applied to two field data sets: one over a known stratigraphic setting and one over an exploration site. The two test sites are both placed in Piedmont, northwest Italy. The first site is located in the Stupinigi area (about 10 km southwest of Torino), while the second one in Villafranca d'Asti (about 40 km southeast of Torino). For all the data sets, simulated or real TDEM and VES soundings were analysed and combined.

The TDEM data are based on the propagation of an induced EM field. For data acquisition, a steady current is forced to flow through a loop for some milliseconds to allow a turn-on transient to be dissipated in the ground. One or more coils, the receivers, are adopted to acquire the response: the transient of the secondary field is a function of the distribution of electrical conductivity in the subsoil. The volume investigated by TDEM is a function of the descending and expanding image of the transmitted current. The electrical resistivity is estimated by analysing the transient decay of the secondary field (McNeill 1990). The basic interpretation of TDEM data is a 1-D resistivity profile under the receiver position. The method is sensitive mainly to conductive formations and, therefore, it is used to extend their evidences with respect to aquifer formations.

The VES is an electric method that deploys two potential electrodes that measure the electric field induced by two current electrodes. The depth of investigation depends on the configuration of the electrodes and the spacing between the current electrodes. The measurements are typically displayed as apparent resistivity (ρ_{app}) as function of the current-electrode half-spacing. Despite VES being one of the oldest geophysical methods, it is still considered worthy due to the efficiency of the set-up and the sensitivity to high resistivity contrasts. Moreover, new joint interpretations of vintage data could provide a more complete characterization if combined with new acquisitions.

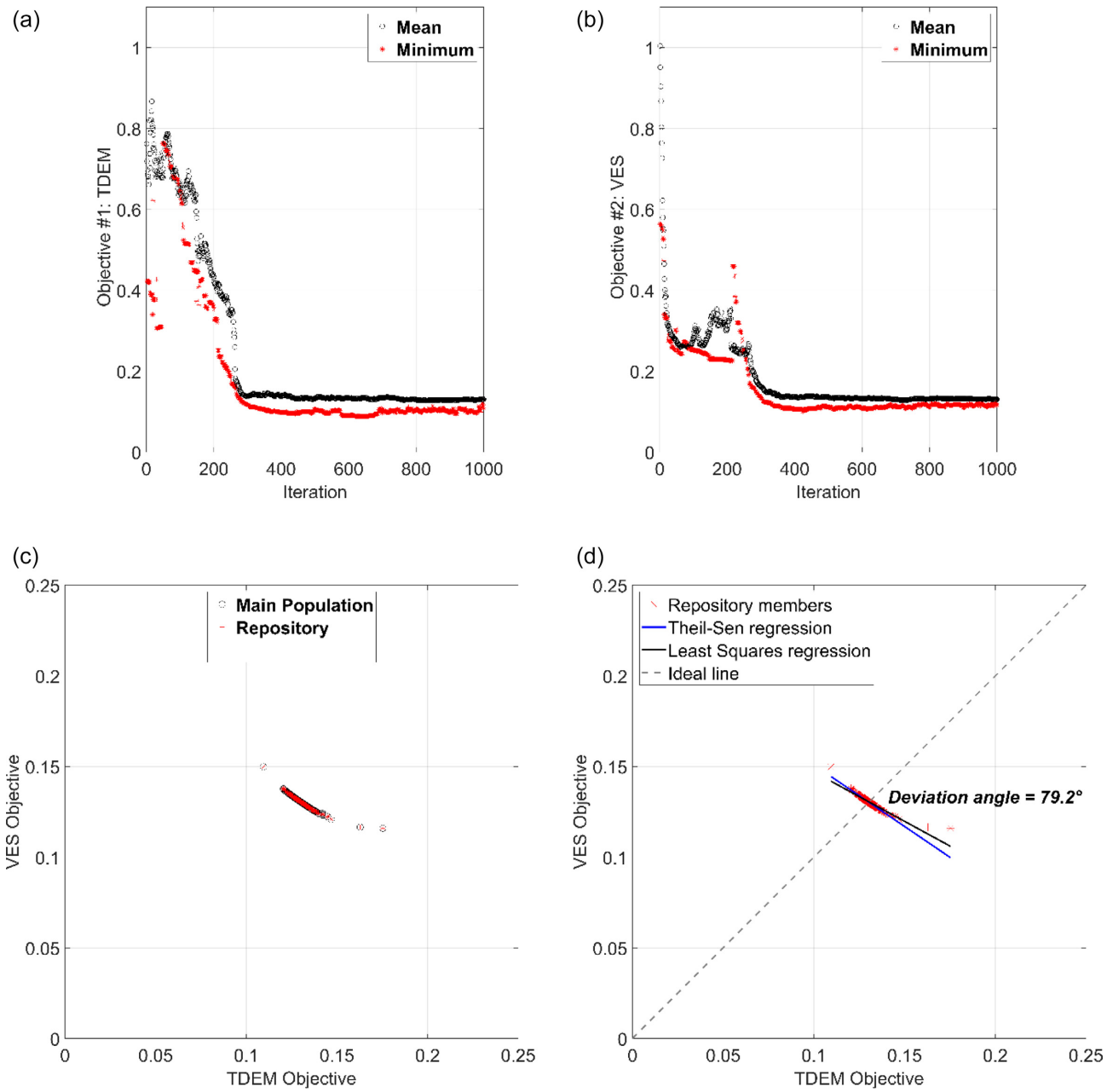

Figure 6. NSGA-III applied to the Stupinigi data set: the evolution of the TDEM (a) and VES (b) components of the objective function from the first to the last iteration for the best individuals (the red stars) and the remaining ones (the black circles); (c) the 2-D space of the objective function (TDEM and VES components) at the last iteration: the red symbols identify the *PF*, while the black circles the objective-function values assumed by the other solutions; (d) the intersection between the ideal line (grey dashed) and the Theil–Sen regression line (blue) or the least-squares regression line (black) identifies the deviation angle α.

3.1 Test on synthetic data

The MOPSO was first tested on synthetic data. The synthetic test model was composed of five layers of different resistivity. The 1-D model is shown in Fig. 2(c) with a red-dashed line, while the TDEM and VES curves are marked with the red dots in Figs 2(a) and (b), respectively. These curves were computed using the forward solvers mentioned before and adopted for the optimization. The error bars refer to 10 per cent Gaussian noise added to the data.

The model solution was discretized into 19 layers and its maximum depth was consistent with the concept of electromagnetic diffusion depth. The application of the L-curve criterion identified the optimal Lagrange multipliers equal to 0.1 for TDEM and 0.01 for VES. The boundary conditions of the search space of solutions were 1 and 500 ohm-m. The TV-MOPSO stopped after 1000 iterations and the outcome is presented in Fig. 2. On the left (Figs 2a and b), the blue lines represent the calculated responses satisfactory fitting the synthetic curves. Fig. 2(c) displays the final result (the blue line) compared to the true model (the red-dashed line) and the other optimized solutions belonging to the *PF* (the green lines). Table 1 lists other details of the optimization, such as: the *RI* (eq. 8), the *SP* (eq. 9), the angle α (eq. 10), the total runtime (in hours), the data misfit and model misfit calculated as the root-mean-square

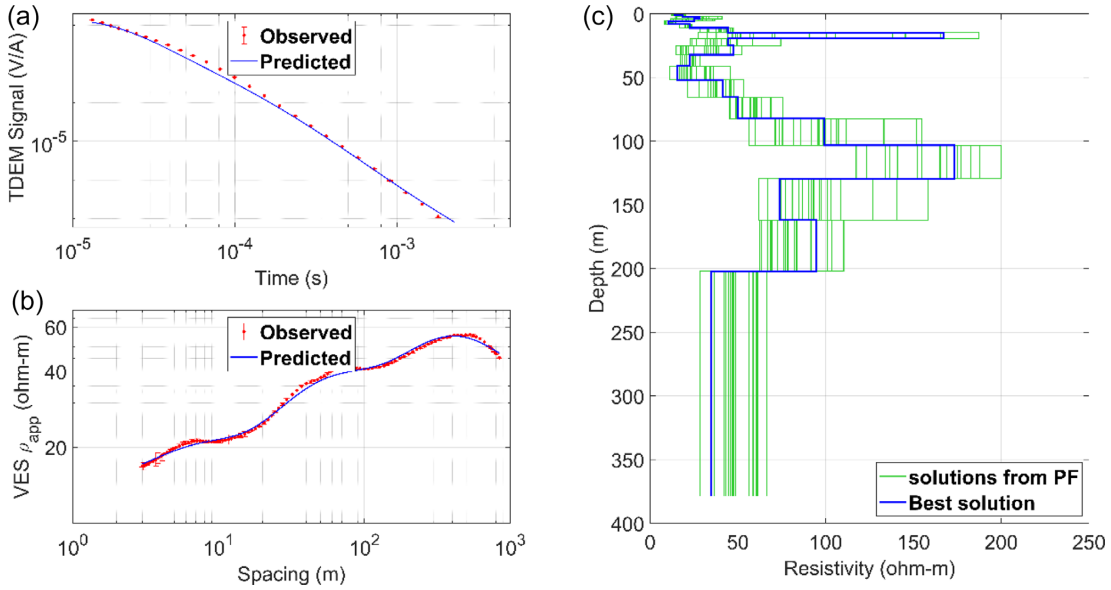

Figure 7. The result of TV-MOPSO applied to the Villafranca data set: observed data (the red dots with error bars) and predicted apparent resistivity (ρ_{app}) for TDEM (a) and VES (b) data; (c) the final resistivity models belonging to the *PF* (the green lines) and the best solution highlighted in blue.

error normalized by the mean value (NRMSE). The graphic representation of the performance of the algorithm (i.e. the objective minimization, the *PF*, etc.) will be shown for the real data sets.

3.2 Stupinigi test site

The site of Stupinigi was chosen to assess the reliability of the suggested method. The area is characterized by a well-known lithological and stratigraphic sequence and a flat morphology. From a geological perspective, the site lies on an alluvial plain, characterized by sand and gravel deposits. The uppermost formation is composed of recent coarse gravel deposits and is followed by an alternation of gravel and sand (well consolidated and cemented) up to hundreds of meters of depth. These two formations constitute two different aquifers separated by embedded clayey layers.

The TDEM data have been acquired using a coincident-loop configuration with a 50-m-long loop for both the transmitter and receiver. The injected current was equal to 3 A, the turn-off time was 4 μs, and a total of 27 samples were acquired in the range between 10^{-5} and 10^{-3} s. The VES have been collected according to a Schlumberger array and deploying a 100 m maximum half-spacing of the current electrodes. The observed ρ_{app} and the corresponding error bars for TDEM and VES are plotted with the red dots in Figs 3(a) and (b), respectively. The TDEM measurements had the correspondent uncertainties associated with the data, while the errors of VES data were not available and hence assumed by adding 10 per cent of Gaussian noise.

A preliminary analysis of the data was performed to assess the compatibility between the electrical and electromagnetic sounding curves. It is known that VES curves may be affected by electrical static shift, or galvanic distortion, that must be identified and removed before the joint inversion. We adopted the scaling relationship of Meju (2005) to compare, on one hand, the VES apparent resistivity curve as a function of the equivalent TDEM delay time and, on the other hand, the TDEM apparent resistivity curve transformed from the signal as a function of the delay time. The presence of a vertical displacement between the VES and TDEM curves is generally regarded as the proof of static-shift occurrence. Conversely, a good parallelism means that the data are compatible and suitable for 1-D joint inversion (Meju 2005). This preliminary analysis proved that there was no vertical displacement of the curves and hence the 1-D joint optimization could be carried out.

The maximum depth of investigation granted by the half-spacing of VES electrodes was about 60 m. Keeping this value for the validity of the interpretation, we extended the maximum depth of the model up to 110 m to graphically represent the half-space. The model was discretized into 19 layers, whose thickness increased logarithmically with depth. Once the L-curve criterion was applied, the optimal Lagrange multiplier was set equal to 0.1 for both TDEM and VES components of the objective function. The boundary conditions of the solution search space were the minimum and maximum resistivity values of 1 and 500 ohm-m, respectively. The MOPSO algorithm ran for 1000 iterations, giving in the end the family of the resistivity models, or Pareto-optimal solutions, plotted in Fig. 3(c). The solutions drawn from the *PF* are depicted in green, while the blue line corresponds to the solution with the minimum value for both the components of the objective function. As visible from Figs 3(a) and (b), the fitting between the observed ρ_{app} and calculated response is remarkable for both TDEM and VES, respectively. The model displayed in Fig. 3(c) reveals a resistive layer of about 200 ohm-m in the shallow subsurface, till 10 m of depth. A conductive region of less than 50 ohm-m appears from a depth of about 20–40 m, while, at higher depths, the resistivity increases to 77 ohm-m.

Figs 4(a) and (b) show on separate plots the contextual minimization of the two components of the objective function (TDEM and VES, respectively) from the first to the last iteration: the red stars correspond to the particles with the minimum $f_j(\boldsymbol{m})$, while the black circles to the mean $f_j(\boldsymbol{m})$ among the remaining particles, that is, solutions found. Fig. 4(c) displays the 2-D space of the objective function at the final iteration. The black circles represent the $f_j(\boldsymbol{m})$ of the particles forming the swarm, while the red stars highlight the *PF*, that is, the $f_j(\boldsymbol{m})$ of the non-dominated solutions stored in the repository. The *PF* was assayed using the metrics reported in eqs (8), (9) and (10). The *RI* was 21.5 per cent, the *SP* was 0.0041 and the deviation angle α was 78.9°, as listed in Table 2. Fig. 4(d)

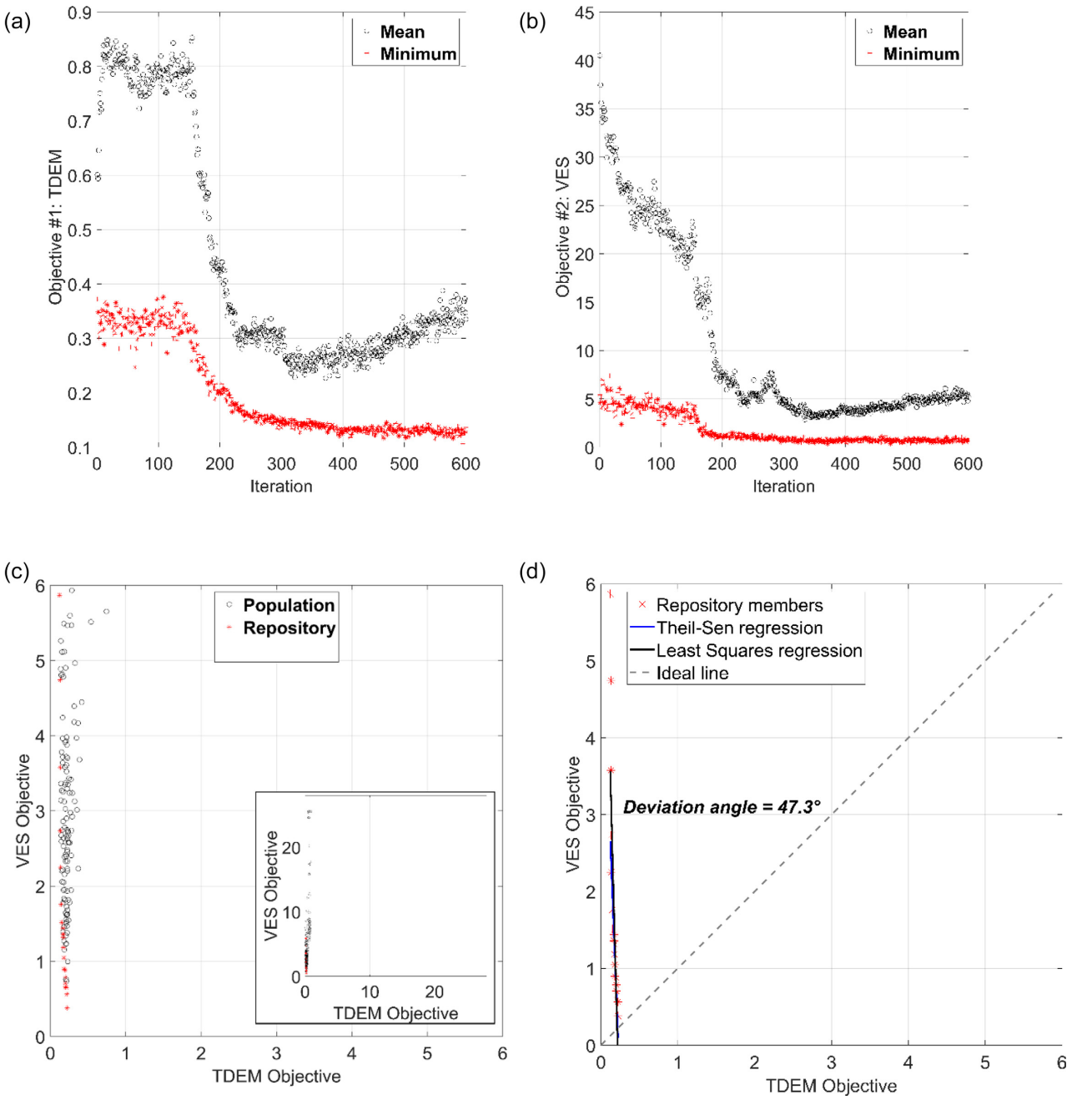

Figure 8. TV-MOPSO applied to the Villafranca data set: the evolution of the TDEM (a) and VES (b) components of the objective function from the first to the last iteration for the best particle (the red stars) and the remaining ones (the black circles); (c) the 2-D space of the objective function (TDEM and VES components) at the last iteration: the red symbols identify the *PF* and the black circles the objective-function values assumed by the other solutions; (d) the intersection between the ideal line (grey dashed) and the Theil–Sen regression line (red) or the least-squares regression line (blue) identifies the deviation angle α.

zooms in the *PF* that gave the deviation angle between the grey-dashed ideal line and the Theil–Sen-regression blue line over the non-dominated solutions. As previously explained, $\alpha > 45°$ proved data incompatibility (Schnaidt *et al.* 2018) and a slight conflict between TDEM and VES was inferred from the asymmetric shape of *PF* (Dal Moro & Pipan 2007).

The resistivity model obtained using NSGA-III is shown in Fig. 5(c), together with the satisfactory match between TDEM and VES observed data and computed response of Figs 5(a) and (b), respectively. The model appears considerably similar to that of Fig. 3(c). The most apparent correspondences are the resistive layer in the shallow subsurface (about 200 ohm-m) and the conductive region (with the minimum 20 ohm-m) from 20 to 40 m of depth. The main difference from Fig. 3(c) is the evident similarity among the non-dominated solutions (the green lines of Fig. 5c), which will be discussed later.

The performance of the algorithm can be analysed from Fig. 6. Figs 6(a) and (b) show how, at the end of the optimization, both the TDEM and VES components converged towards the minimum

Table 3. Analysis of the performance of MOPSO and NSGA-III on the data set from Villafranca. The rows report the number of iterations run, repository index (*RI*), spacing (*SP*), deviation angle (α) between the ideal and Theil–Sen regression line, total runtime in hours and normalized root-mean square error (NRMSE) for TDEM and VES.

Villafranca data set	MOPSO	NSGA-III
Iterations	600	1000
RI (per cent)	12.4	100
SP	0.3584	0.0164
α (°)	47.3	46.7
Runtime (h)	7.1	10.8
NRMSE TDEM	0.173	0.2009
NRMSE VES	0.0272	0.0384

value of the objective function, which is found by the best individuals of the population (the red stars). Like Figs 4(a) and (b), the objective decreased by more than 80 per cent after about 400 iterations, but the effective minimization was reached in 1000 iterations. At the end, the objective space hosted the *PF* plotted in Fig. 6(c) with the red stars that are coincident to the black circles because all the population corresponded to non-dominated solutions, thus giving $RI = 100$ per cent. The Theil–Sen regression line identified a deviation angle of 79.2° with the ideal line (Fig. 6d), in line with that of MOPSO (see Table 2). The NRMSE was calculated for the results of MOPSO and NSGA-III, as listed in Table 2.

3.3 Villafranca test site

The second case study is located in Villafranca d'Asti, where a large well-field extensively exploits a confined aquifer to supply drinking water to 43 municipalities within the Asti Province (De Luca *et al.* 2018). The exploited aquifer consists of Pliocene marine deposits (mainly 'Asti Sands' formation) bounded at the base by a Pre-pliocene marine complex, consisting of silty–clayey sediments, and by a Lower-Middle Pliocene marine complex (represented by the Lugagnano Clay), consisting of sandy–marly clay, upward intercalated with coarser sediments (De Luca *et al.* 2014; Lasagna *et al.* 2014). Both these lower complexes have a very low or negligible permeability and represent an aquiclude, under the overlying Asti Sands. By contrast, the Asti Sands are sandy sediments, alternated with levels of fine sand, sandy–gravel, clayey sand, silty–sandy and silty–clayey levels with very low permeability. The alternation between mainly sandy sediments with a good permeability and poorly permeable levels makes this complex a multilayered aquifer system, in which the various aquifer levels can intercommunicate through semipermeable levels.

A geophysical survey has been carried out in the area to better understand the formation of this aquifer layer and potentially identify new positions for water wells (De Luca *et al.* 2018). Within the performed surveys, acquisition of TDEM data has been carried out using a coil size of 100 × 100 m for the transmitter, and both 0.6 × 0.6 m (20 turns) and 10 × 10 m (2 turns) receiver coils for the receiver, located at the centre of the transmitter coil. TDEM transient curve has consisted of 40 measuring points, from 1.2×10^{-6} to 8.8×10^{-3} s. Injected current has been around 10 A and a stacking of 2000 measurements has been performed. The acquisition has been carried out using an ABEM WalkTEM instrument. Several of these soundings have been performed over the area and then globally inversed with a spatially constrained inversion (SCI) algorithm (De Luca *et al.* 2018). In our study, a single TDEM sounding was integrated with one VES sounding. The available vintage VES acquisition has been performed using the Schlumberger configuration with a maximum half-spacing of about 850 m between the current electrodes (Città di Asti 1962). As in the Stupinigi case study, the TDEM measurements had the original uncertainties associated with the data, while the errors of VES data were assumed by adding 10 per cent of Gaussian noise. This may be regarded as the contribution of the original experimental errors, the possible inaccuracy of the conversion from the original data to the digital form and the inaccuracy of editing and smoothing apparent resistivity curves.

VES and TDEM curves were preliminary analysed to infer the possible occurrence of the electrical static shift. After applying the scaling relationship of Meju (2005), we verified that the two data sets were acceptably compatible for joint inversion.

In the MOPSO algorithm, the lower and upper boundaries of the search space were fixed at 1 and 200 ohm-m, respectively. The application of the L-curve criterion identified the optimal Lagrange multipliers equal to 0.1 for TDEM and 10^{-4} for VES. The results from MOPSO are presented in Fig. 7. On the left, the fitting between observed (the red error bars) and calculated (the blue line) data is noteworthy for both TDEM signal (Fig. 7a) and VES apparent resistivity (Fig. 7b). On the right, Fig. 7(c) displays the set of Pareto-optimal solutions in green and the selected one with the minimum components of $\boldsymbol{f(m)}$ in blue. The 1-D vertical profile was composed of 19 layers, up to a maximum depth of about 380 m. The family of non-dominated solutions reveals two resistive regions: the first overcomes 100 ohm-m in the shallow subsurface (about 20 m of depth); the second ranges from 100 ohm-m to 200 ohm-m at a depth from about 50 to 150 m. This last resistive layer may be related to the confined aquifer object of the investigation in the area, as mentioned before.

The MOPSO ran for 600 of 1000 iterations since the repository was not filled for 300 consecutive iterations (second stopping criterion). Figs 8(a) and (b) plot the trend, iteration after iteration, of the TDEM and VES components of the objective function, respectively. At the final stages of the optimization, the mean $f_j(\boldsymbol{m})$ (the black circles) slightly increased, but the minimum $f_j(\boldsymbol{m})$ (the red stars) showed convergence. At the last iteration, the *PF* took the shape shown in Fig. 8(c) with the red stars. The objective-function values of the other particles of the swarm are marked with the black circles. The zoom-in box reveals a complete view of the search space and, in particular, the wide range of the VES-component values for the particles outside the repository. The metrics for the solution appraisal are listed in Table 3: the *RI* was 12.4 per cent and the *SP* was 0.3584. The deviation angle of 47.3° is highlighted in Fig. 8(d) between the Theil–Sen regression and ideal line, that is, the blue and grey-dashed lines, respectively. The vertical shape of the *PF* as well as the α slightly greater than 45° suggested a partial compatibility between the data sets.

The benchmark algorithm NSGA-III was applied to the Villafranca data set yielding the outcome illustrated in Fig. 9. Fig. 9(a) shows the appreciable match between observed TDEM signal (the red dots) and calculated response (the blue line), while Fig. 9(b) reports an acceptable fitting for the VES ρ_{app}. The non-dominated solutions drawn from the *PF* are plotted in green in Fig. 9(c) and the selected blue model does not present significant differences from them. A resistive body with a peak of 130 ohm-m is imaged at about 10–15 m of depth, while from 50 to 100 m of depth the resistivity increases up to a maximum of 85 ohm-m. Then, it gradually decreases to 50 ohm-m.

The performance of NSGA-III can be read from Fig. 10 and Table 3. A total of 1000 iterations were requested for a robust

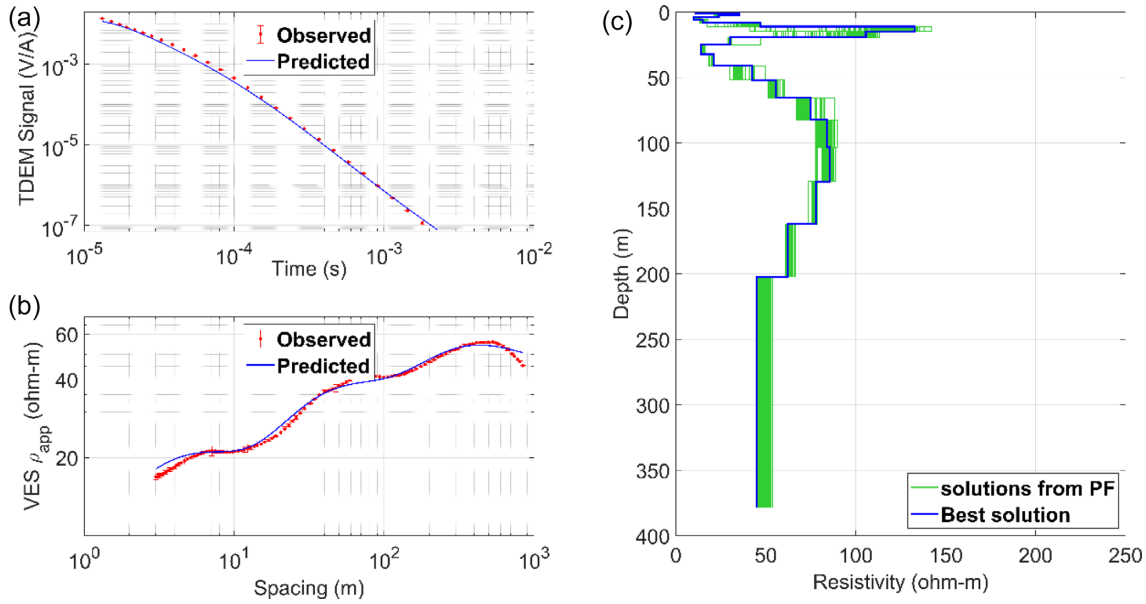

Figure 9. The result of NSGA-III applied to the Villafranca data set: observed data (the red dots with error bars) and predicted apparent resistivity (ρ_{app}) for TDEM (a) and VES (b) data; (c) the final resistivity models belonging to the *PF* (the green lines) and the best solution highlighted in blue.

minimization of both components of the objective function. Even though Figs 10(a) and (b) show a decreasing trend, the mean value of the VES component (the black circles in Fig. 10b) was two orders of magnitude larger than the corresponding TDEM. However, at the end of the optimization, the minimum values of the TDEM and VES components were quite similar, as depicted in Fig. 10(c). It is the snapshot of the objective space at the last iteration. All the population members were evaluated as non-dominated solutions and hence the corresponding objective-function values were marked with the black circles and the red symbols at the same time (*RI* = 100 per cent). The *PF* is plotted with the red stars in Fig. 10(d) to highlight the deviation angle $\alpha = 46.7^{\circ}$ between the Theil–Sen regression blue line and the grey-dashed ideal line. The NRMSE is reported in Table 3 for the results from MOPSO and NSGA-III.

4 RESULTS FROM THE SINGLE-OBJECTIVE SEPARATE OPTIMIZATIONS

This section presents the separate optimizations of the synthetic and real data sets using the single-objective PSO. The input parameters of the algorithm were kept as previously explained: the model was discretized into 19 layers, the swarm was composed of 170 particles and the L-curve criterion identified the optimal the Lagrange multiplier. Since the process of separate optimization is simpler than the MO problem, few iterations were required to gain the solution convergence. The PSO algorithm ran for a maximum of 500 iterations or stopped before if the fitness functions did not minimize for 100 consecutive iterations (second stopping criterion). Each run was launched 10 times (or 'trials') in order to test the solution variability coming from the initial random distributions. Santilano *et al.* (2018) indeed proved for 1-D MT that different random initializations of the model resulted in highly comparable but not identical final solutions. The MOPSO was not launched for different trials because the dominance criterion exercised, among the possible solutions, the same selective choice performed by several trials of single-objective PSO. In MOPSO, the best-solution selection is a mathematically refined process, while in simple PSO it is based on the straightforward minimization of a single objective. The solution with the minimum NRMSE among the 10 solutions was eventually selected as the best optimized model. The boundary conditions of the search space of the solutions were kept as reported in the previous paragraphs for the two data sets, respectively. The simulations have been run by adopting only two workers of the HPC cluster because unnecessary computational resources were not allowed. For this reason, the comparison between the MO and single-objective optimizer could not be assessed in terms of runtime.

For the single-objective PSO of synthetic data, the Lagrange multiplier was 10^{-3}. The best trial of TDEM optimization ran for 398 iterations and the corresponding predicted response and final resistivity model are plotted in blue in Figs 11(a) and (b), respectively. The outcomes from the other trials are marked in green, while the true model in red. The final NRMSE of the data fitting was 0.0277 and of the model fitting was 0.4445 (Table 4). The best result from PSO of VES synthetic data, after 419 iterations, is shown in Fig. 12 and gave a final NRMSE of 0.0065 as data misfit and of 0.27 as model misfit (Table 4).

As regard the Stupinigi site, the Lagrange multiplier was 10^{-3} and the best trial ran for 500 iterations. The response from PSO of TDEM data is shown in Fig. 13. Fig. 13(a) plots the significant match between the observed data (the red dots and error bars) and the calculated response (the blue line) from the best model. It is marked in blue in Fig. 13(b) and the solutions from other trials in green. All the models concur in identifying a conductive region of about 30 ohm-m between 20 and 40 m of depth. Table 4 lists the final NRMSE of 0.0791.

The trend of the optimization is visible in Fig. 14. Fig. 14(a) plots the decrease of the objective function (*f(m)*) from the first to the last iteration as assumed by the best particle (the black dots) and the mean value of the remaining particles (the blue dots). Fig. 14(b) represents the value of *f(m)* assumed by the particles as a function of their position in the first two layers of the model (represented by the two horizontal axes): the grey dots reveal the initial random positions of the particles, while the red-circled blue dot is the final

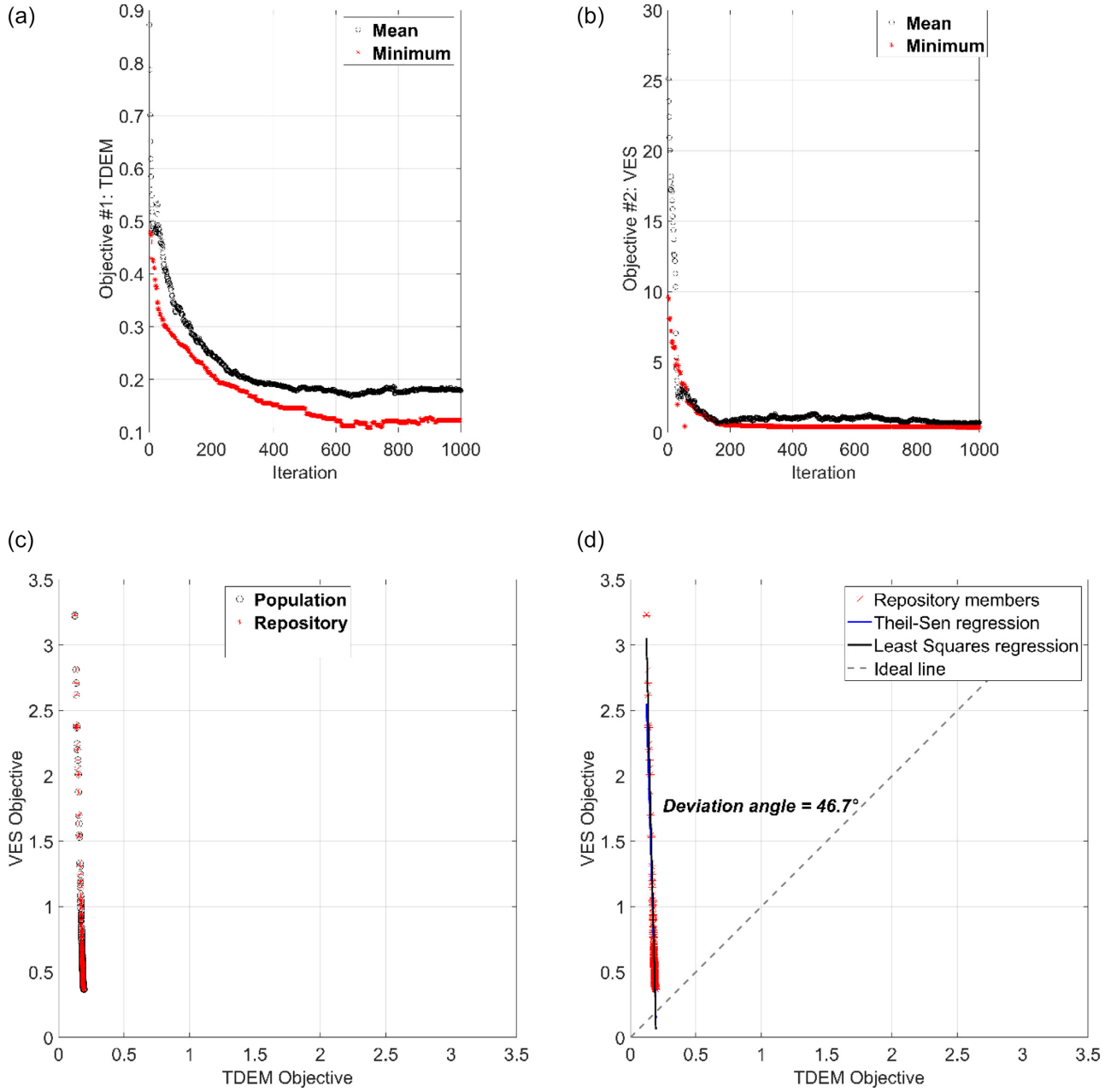

Figure 10. NSGA-III applied to the Villafranca data set: the evolution of the TDEM (a) and VES (b) components of the objective function from the first to the last iteration for the best individuals (the red stars) and the remaining ones (the black circles); (c) the 2-D space of the objective function (TDEM and VES components) at the last iteration: the red symbols identify the *PF*, while the black circles the objective-function values assumed by the other solutions; (d) the intersection between the ideal line (grey-dashed) and the Theil–Sen regression line (red) or the least-squares regression line (blue) identifies the deviation angle α.

position of the whole swarm at convergence. Fig. 14(c) is the plain view of Fig. 14(b) and highlights the random initialization of the particles (the grey dots). The bar plot of Fig. 14(d) displays how many particles had the same *f(m)* at the end of PSO.

The response from PSO of VES data is shown in Fig. 15. Fig. 15(a) plots the significant match between the observed ρ_{app} (the red dots and error bars) and the calculated response (the blue line) from the best model, which is marked in blue in Fig. 15(b). Excepting one trial, the remaining models (the green lines), are highly comparable and image a resistive body of about 180 ohm-m at about 5 m of depth. Table 4 lists the final NRMSE of 0.0288.

The independent optimizations of TDEM and VES from the Villafranca data set spawned the results of Figs 16 and 17, respectively. The predicted TDEM signal of Fig. 16(a) is not dissimilar to the observed data marked with the red dots and error bars. The resistivity models of Fig. 16(b) are plotted in green, while the best trial is marked in blue and was obtained after 325 iterations. The model shows a slight decrease of resistivity from 10 to 25 m of depth and then at 40 m deep an increase from 20 to 80 ohm-m. The NRMSE was 0.2106, as listed in Table 4. The VES ρ_{app} was distinctly matched after 421 iterations as reported in Fig. 17(a). The observed ρ_{app} is plotted with the red dots and without the error bars because the measurements were resampled on the original

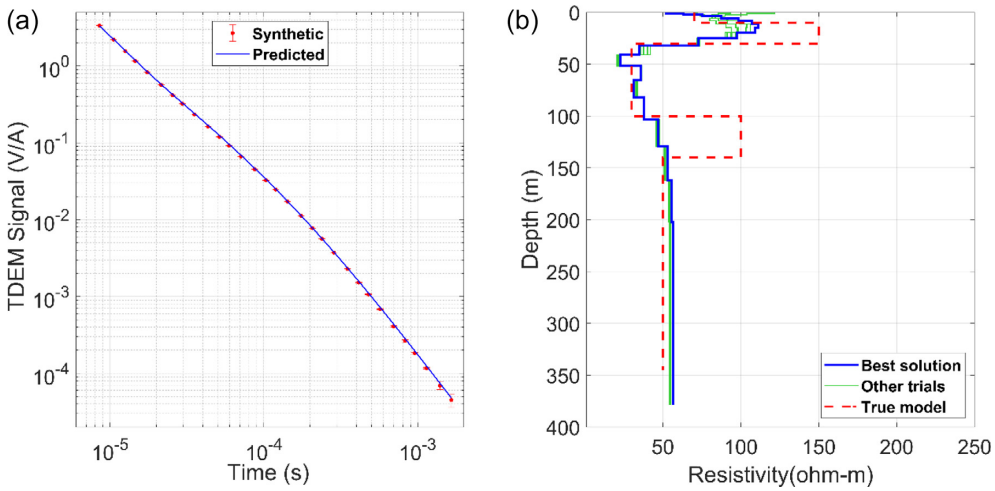

Figure 11. Single PSO of TDEM synthetic data. (a) fitting between observed signal (the red dots and error bars) and predicted response (the blue line); (b) the red-dashed line is the true model, the green lines correspond to the resistivity models from different PSO trials, while the blue line is the best solution.

Table 4. Analysis of the performance of single-objective PSO on the synthetic, Stupinigi and Villafranca data sets. The columns report the method, the number of iterations run, the normalized root-mean square error (NRMSE) and the runtime of a single trial (in minutes').

	Method	Iterations	NRMSE	One-trial runtime(')
Synthetic test	TDEM	302	0.0299 (data)0.4276 (model)	122.45
	VES	465	0.0053 (data)0.2621 (model)	2.6
Stupinigi data set	TDEM	500	0.0791	21.37
	VES	500	0.0288	1.48
Villafranca data set	TDEM	325	0.2106	84.86
	VES	421	0.0148	3.61

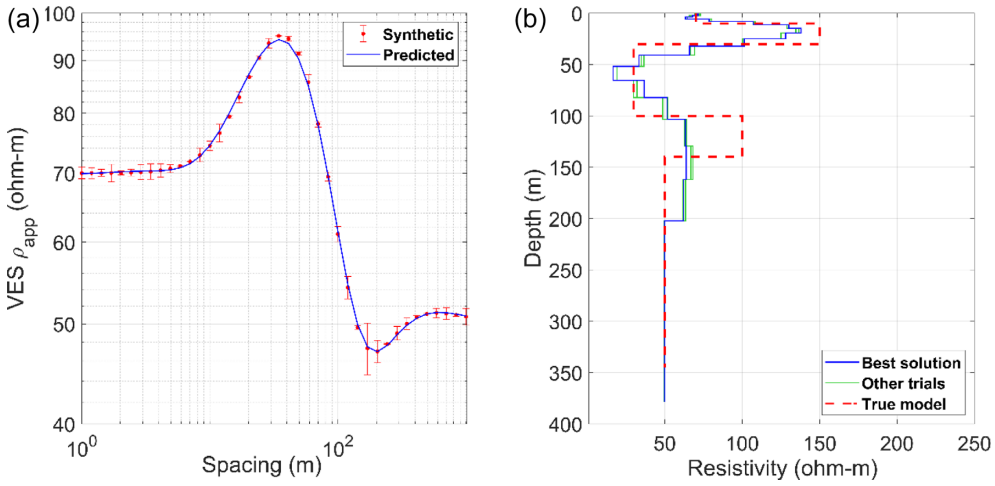

Figure 12. Single PSO of VES synthetic data. (a) fitting between observed apparent resistivity ρ_{app} (the red dots and error bars) and predicted response (the blue line); (b) the red-dashed line is the true model; the green lines correspond to the resistivity models from different PSO trials, while the blue line is the best solution.

smoothed curve, thus making ambiguous any consideration about errors. Fig. 17(b) shows the solutions obtained after the 10 trials: the best trial is plotted in blue and gave an NRMSE of 0.0148 (Table 4). The best model images in top-down order: a resistive subsurface of about 90 ohm-m, a conductive break with the minimum 6 ohm-m at about 30 m of depth and a deep resistive region of about 100 ohm-m.

5 DISCUSSION

Our novel joint-optimization algorithm was first validated on a synthetic example. The true model was conceived in some ways similar to the experimental data to be tested. The MOPSO outcome was largely consistent with the true synthetic model, thus demonstrating

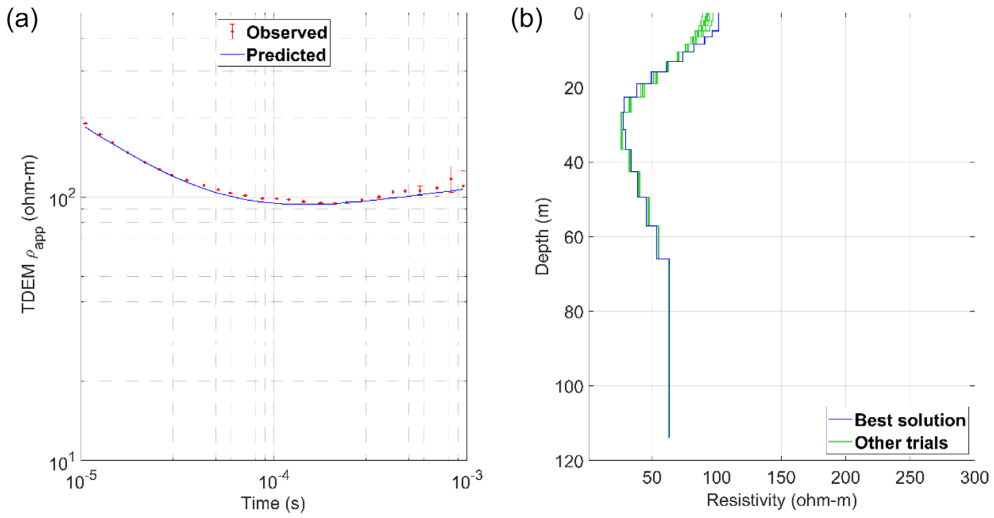

Figure 13. Single PSO of TDEM measurements at Stupinigi site. (a) fitting between observed apparent resistivity ρ_{app} (the red dots and error bars) and predicted response (the blue line); (b) the resistivity models in green correspond to the different PSO trials, while the best solution is marked in blue.

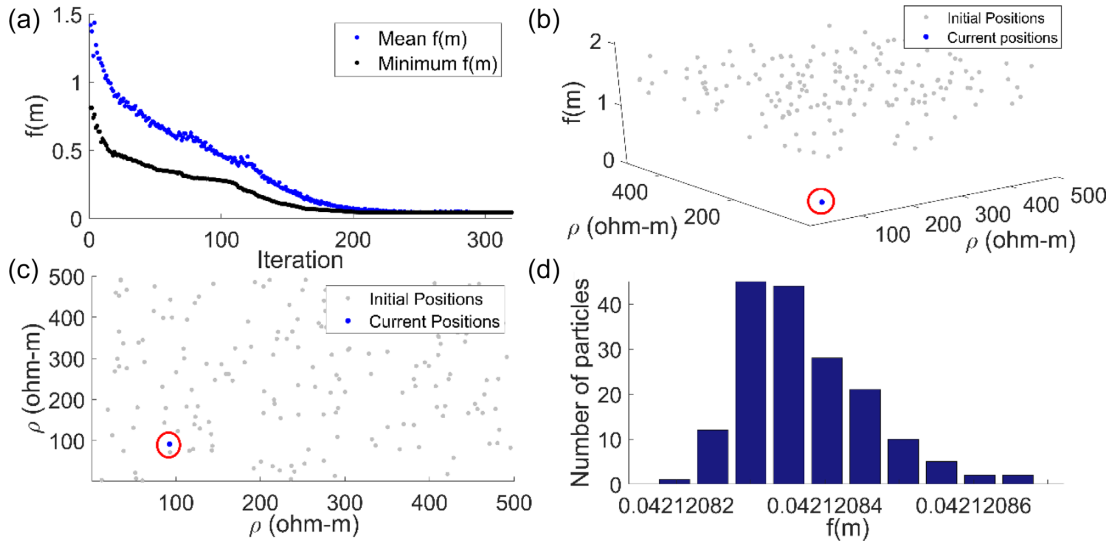

Figure 14. PSO performance at the end of the optimization: (a) the decrease of the fitness function, iteration after iteration, for the best particle (the black dots) and the remaining swarm (the blue dots); (b) the fitness-function value as a function of the particle positions in the resistivity (ρ) search space, at the first (the grey dots) and final (the red-circled blue dots) iterations; (c) plain view of (b); (d) final distribution of the fitness-function values among all the particles.

its applicability to real data. The validity of the synthetic test was also evident from the model misfit: the one of MOPSO (Table 1) was lower than those of the single optimizations (Table 4). By contrast, the data misfits from the single optimizations (Table 4) were a little lower than those from MOPSO, but this was not surprising. It is reasonable to assume that the interpretation of both TDEM and VES information limited the data fitting but yielded a better definition of the final model (i.e. lower model misfit).

The general overview of the results coming from the MOPSO and NSGA-III algorithms suggests some preliminary comments. The objective-function components were iteratively minimized according to a sharp slope at the early stages and, later, a flat trend (see a and b of Figs 4, 6, 8 and 10). This happened because of the initial heterogeneity and the significant changes from one iteration to another given by k-dependent coefficients in MOPSO and mutation and crossover in NSGA-III. After that, the largest part of the minimization was overtaken, the models became more homogeneous even though in MOPSO a slight diversity was ensured by the accelerations.

As regards the MOPSO algorithm applied to the Stupinigi data set, the shape of the *PF* and the high deviation angle in Fig. 4(d) suggested data incompatibility. It was actually expected since it is known that a perfect compatibility can be found only for synthetic data (Schnaidt *et al.* 2018) and real-world problems commonly have conflicting objectives (e.g. completing a task in the shortest time and in the cheapest way can be a MO problem with conflicting objectives!). The incompatibility may be attributed to the different depths of investigation: that associated with the VES half-spacing was lower than that of TDEM. This difference resulted because TDEM explores subsurface volumes enlarging with depth according to the principle of the diffusion depth, while VES covers volumes more laterally extended. Despite incompatible, we may conclude that the data were complementary, as shown in Figs 13 and 15: TDEM is more sensitive to the conductive region and VES to the

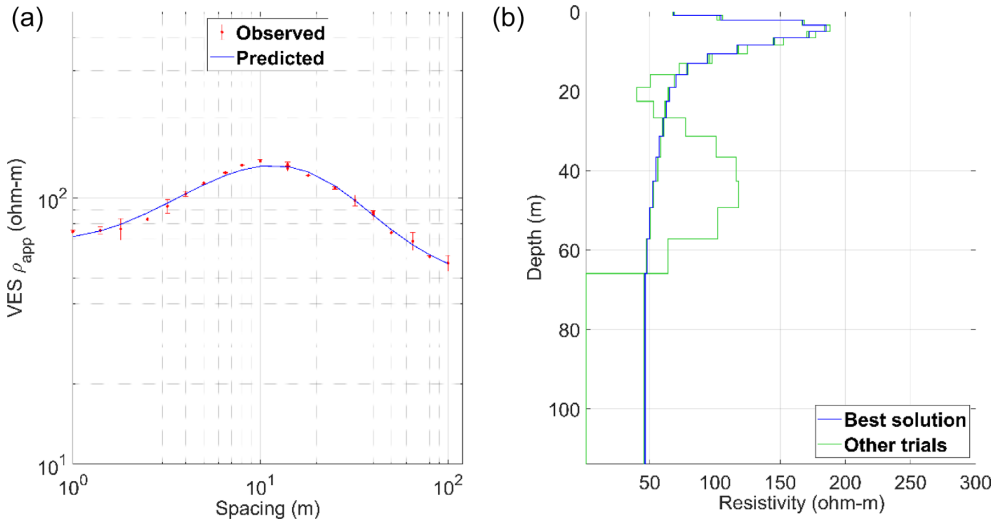

Figure 15. Single PSO of VES data at Stupinigi site. (a) fitting between observed apparent resistivity ρ_{app} (the red dots and error bars) and predicted response (the blue line); (b) the resistivity models in green correspond to the different PSO trials, while the best solution is marked in blue.

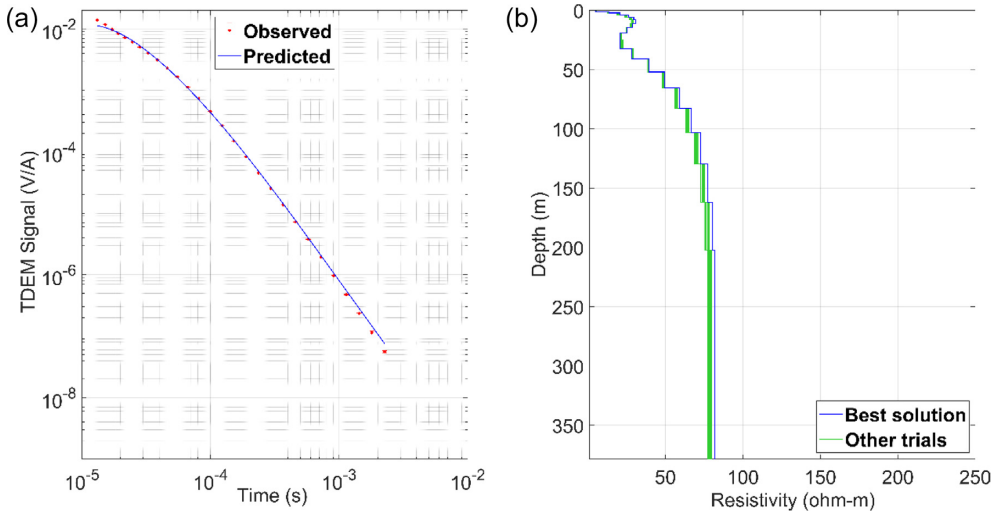

Figure 16. Single PSO of TDEM measurements at Villafranca site. (a) fitting between observed signal (the red dots and the error bars) and predicted response (the blue line); (b) the resistivity models in green correspond to the different PSO trials, while the best solution is marked in blue.

superficial resistive layers. Our results can be directly compared to those obtained from separate Monte Carlo inversions in Piatti *et al.* (2010). This work was a benchmark for our models despite some differences between the two methods: TV-MOPSO deployed a random initialization and then the adaptive behaviour, while the importance sampling method of Piatti *et al.* (2010) exploited the scale property of the apparent resistivity curves to integrate sampling and optimization. Fig. 18 shows the solutions of our joint optimizations with MOPSO (the dashed line) and NSGA-III (the solid line) and Monte Carlo inversion of TDEM (the dotted line) from Piatti *et al.* (2010). This comparison made evidence of the clear advantages of MOPSO: the final model was achieved using a single optimizer for both the data sets instead of separate inversions. The dotted line in Fig. 18 supports the model of Fig. 13 (b) and reveals the limit of the single inversion. Given the same forward-modelling code, Piatti *et al.* (2010) performed 2×10^5 simulations with a three-layer parametrization, while MOPSO ran for 1000 iterations with a 19-layer parametrization. The samplings and the runtime were less than in Piatti *et al.* (2010). Our results are also supported by the geological information derived from a borehole located very close to the investigated site. The stratigraphy is depicted in the right of Fig. 18 and is in good agreement with the inversion results. Particularly, the correspondence between the gravel structure and high-resistivity layers in the shallow subsurface is notable. Our outcomes outperform the result of Piatti *et al.* (2010), which underestimated the superficial resistive structure and overestimated the thickness of the clay layer.

The application of MOPSO to the Villafranca data set offered an insight into data compatibility. Given the maximum half-spacing of the current electrodes (844 m), the VES reached a depth of investigation higher than that of TDEM sounding, which was negatively affected by the superficial conductive region. The deviation angle of $47.3^\circ > 45^\circ$ (Table 3) proved the lack of data compatibility. However, a partial compatibility may be assumed because α was slightly bigger than 45° and the *PF* was almost vertical, as proved by the Theil–Sen regression line that tends to bend towards the *y*-axis (VES component in Fig. 8c). What is more, the models from the separate

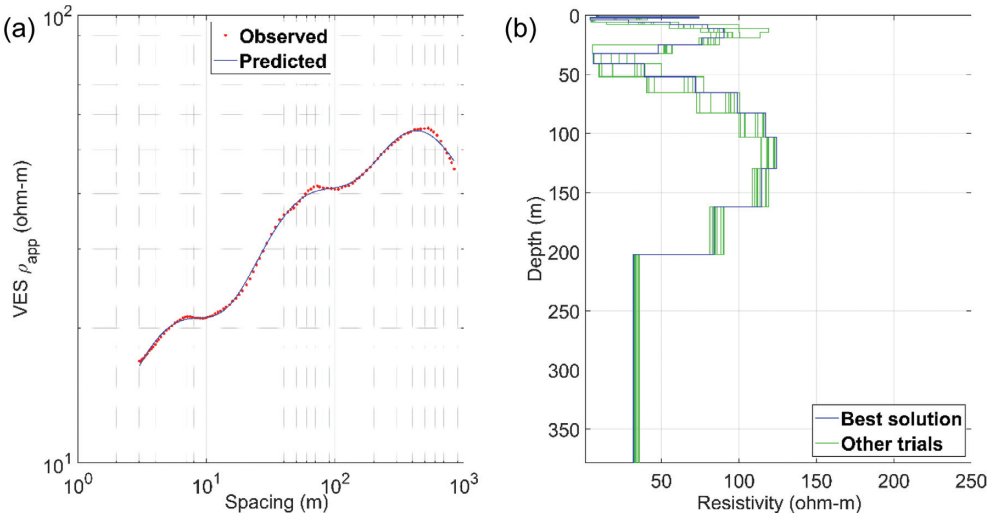

Figure 17. Single PSO of VES data at Villafranca site. (a) fitting between observed apparent resistivity ρ_{app} (the red dots) and predicted response (the blue line); (b) the resistivity models in green correspond to the different PSO trials, while the best solution is marked in blue.

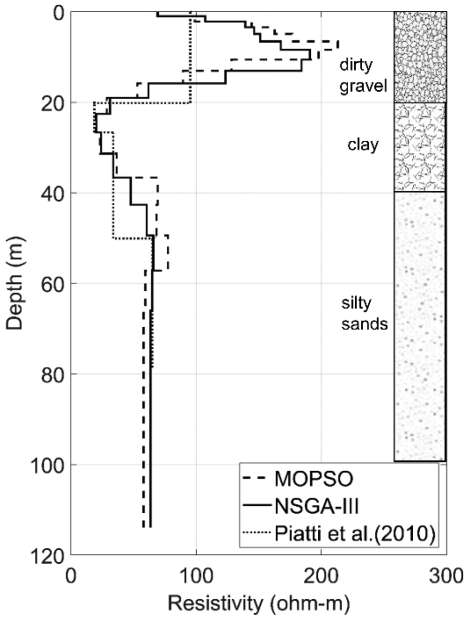

Figure 18. Comparison of the different interpretation of the Stupinigi data set using MOPSO (the dashed line), NSGA-III (the solid line) and Monte Carlo from Piatti *et al.* (2010; dotted line). On the right, the stratigraphy from a borehole placed very close to the sounding.

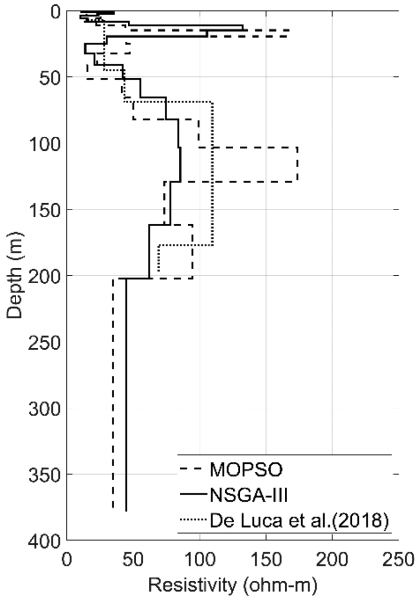

Figure 19. Comparison of the different interpretation of the Villafranca data set using MOPSO (the dashed line), NSGA-III (the solid line) and SCI (the dotted line) from De Luca *et al.* (2018).

optimizations (Figs 16 and 17) were in good agreement on the conductive region at about 40 m of depth. From this depth downwards, the TDEM data lost resolution and hence the trade-off solutions from MOPSO mainly interpreted the information from VES. In fact, Fig. 8(c) showed a clear convergence of the particles on the same value for the TDEM component and, in contrast, a large distribution for the VES components. This explains the vertical shape of the *PF* and the high value of *SP*. Compared to the optimization of the Stupinigi data set, less iterations ran (600 versus 1000) to ensure a significant minimization of the objective function (Figs 8a and b). Even though, at the beginning of the optimization, the VES component of the objective function was two orders of magnitude larger than the TDEM component, they both assumed almost the same value at the final iterations. The resistivity model obtained from the Villafranca data set using the MOPSO algorithm is in line with the results published in De Luca *et al.* (2018) using the same TDEM data set. Fig. 19 gives a direct comparison among the models from MOPSO (the dashed line), NSGA-III (the solid line) and the SCI (the dotted line) from De Luca *et al.* (2018). This last model interprets only TDEM data and hence does not image the superficial resistive layer. All the models are in good agreement about the top and bottom of the deep resistive layer constituting the aquifer. Moreover, the introduction of VES information in the MOPSO inversion allowed a more refined definition of the highest resistive portions of the multilayered aquifer system. From literature, these portions are supposed to be related to the more permeable sandy layers and, therefore, relevant for water exploitation. Unfortunately, there is no availability of geological or geophysical information on this specific site (well logs, seismic, etc.). In fact, this was the reason for the recent geophysical investigations. We can conclude

that we analysed three different case studies with increasing level of uncertainty: the synthetic model was *a priori* known, the Stupinigi model was validated by the stratigraphy and finally, the Villafranca model had no external information to be compared with. However, we here stress on the advantages of the new joint-optimization approach and any geological or lithological interpretation of our result goes beyond the scope of this paper.

A significant novelty of this work is that the results from two different MO algorithms were directly compared with each other. For the Stupinigi case study, both MOPSO and NSGA-III essentially gave the same models (Fig. 18), runtimes and deviation angles (Table 2). For the Villafranca case study, the main similarities were the deviation angles (Table 3) and the models (Fig. 19), even though the deep layer was imaged in NSGA-III less resistive than in MOPSO. A major difference emerging from Table 3 was the total number of iterations to end in convergence; MOPSO required less iterations than NSGA-III. This outcome was not unexpected since in the literature MOPSO has proven a competitive speed of convergence (Kennedy & Eberhart 2001; Coello Coello *et al.* 2004). Another dissimilarity was that the resistivity models from MOPSO presented a slight reciprocal discrepancy (the green plots in Figs 3c and 7c), while all the non-dominated solutions from NSGA-III were quite similar each other (see Figs 5c and 9c). This was also evident from the *SP* index, which in MOPSO was always higher than in NSGA-III. A possible explanation might be the different criteria to keep and ensure the variability and diversity of the non-dominated solutions. It is worth noting the *RI* of both case studies (Tables 2 and 3). Interestingly, it was below 22 per cent for MOPSO and always 100 per cent for NSGA-III, meaning that MOPSO gave less and sparse non-dominated solutions (low *RI* and high *SP*) and, reversely, NSGA-III more and similar ones. This contrast could be attributed to some inner differences in the core of the methods, that is, the main loop of the algorithms: in MOPSO the selection of the leader and the updating of the repository were ruled differently from the NSGA-III's population selection and association to the reference points. Notwithstanding these dissimilarities, the final models from MOPSO were always largely consistent with that from NSGA-III. The NRMSEs reported in Tables 2 and 3 provided compelling evidence that MOPSO outperformed NSGA-III since the data misfit from MOPSO was always lower than that (or at least the same) of NSGA-III.

The results obtained from the single-objective optimization can be schematically appreciated from Table 4. For the real data sets, the TDEM optimization resulted always in longer runtimes and higher NRMS errors for both case studies, while the number of iterations for the Villafranca optimizations was lower than for the Stupinigi optimizations. The models resulting from the several trials were always in good agreement with each other, excepted for an outlier of little significance in Fig. 15.

6 CONCLUSIONS

This study set out with the aim of providing a new evolutionary method for the joint optimization of different geophysical data sets. The MO problem was solved using a pure MOO called MOPSO, which had hitherto been little applied to geophysics. The problem of possible conflicting solutions was solved by adopting the Pareto optimality. The data sets were TDEM data and VES, resulting in a bi-objective problem. The MOPSO was tested for synthetic data and two different sites placed in northwest Italy. The synthetic example provided a first evidence of the validity and advantage of the MOPSO. The model misfit, measuring the correspondence to the reference model, was lower than the model misfits calculated from the separate optimizations.

For the field data sets, the performance of MOPSO was compared to that of a commonly used GA, the NSGA-III. In general, both MOPSO and NSGA-III revealed a number of attractive features: a single tool to tackle multiple data sets, a set of final models without multiple conflicting solutions and because of the Pareto optimality, an effective insight in the trade-off meaning of the final solutions. In fact, the best trade-off solutions and their range were identified as final solutions because of the Pareto dominance. We also analysed the shape of the *PF* to infer the compatibility between different geophysical data sets. Even in the case of a proven data incompatibility, the separate optimizations with single-objective PSO showed the complementarity of the data sets and hence the validity of the joint-optimization results. Their comparison with stratigraphic information coming from boreholes, when available, corroborated our findings. Therefore, we conclude that the *PF* is fundamental to understanding the limits of joint inversion and the reliability of its outcomes.

Although the long computation time could be seen as a minor drawback, it must be borne in mind that the stochastic nature of the algorithm requires many forward-modelling calculations that result in a significant computational load. We managed the computationally demanding nature of the global search algorithms using the HPC cluster provided by our University. However, we are aware that there is room for improvement and, given the current striking progress in computational efficiency, we are confident this issue will be addressed in future investigations.

The most important finding to emerge from the analysis was that the resistivity models obtained from MOPSO were fully comparable to the ones from NSGA-III, thus supporting the validity of the new proposed method. It can be concluded that MOPSO outperformed the NSGA-III given: the higher speed of convergence in one of the two tests, the more selective filling of the repository and wider variability of the non-dominated solutions (due to an effective exploration of the search space).

Future developments will extend the suggested method to other geophysical data sets whose compatibility may be more easily achievable (e.g. TDEM and controlled-source AMT data). A challenging research opportunity could be the investigation of more than two data sets, thus leading to a 3-D Pareto space.

ACKNOWLEDGEMENTS

Computational resources provided by hpc@polito (http://hpc.polito.it). Acquisition of data in the Villafranca test site was funded by the water management authorities (ATO 5–Ambito Territoriale Ottimale n.5 Astigiano Monferrato). The work of coauthor AS was funded in the framework of the H2020 GEMex Project under the grant agreement 727550.

REFERENCES

Akca, I., Günther, T., Müller-Petke, M., Başokur, A.T. & Yaramanci, U., 2014. Joint parameter estimation from magnetic resonance and vertical electric soundings using a multi-objective genetic algorithm, *Geophys. Prospect.,* **62**(2), 364–376.

Candansayar, M.E. & Tezkan, B., 2008. Two-dimensional joint inversion of radiomagnetotelluric and direct current resistivity data, *Geophys. Prospect.,* **56**(5), 737–749.

Cheng, F., Li, F., Peng, S., Sun, X., Zheng, J. & Jia, Z., 2015. Joint inversion of TEM and DC in roadway advanced detection based on particle swarm optimization, *J. Appl. Geophys.,* **123,** 30–35.

Città di Asti, Ricerche Idriche, 1962. Studio Idrogeologico e prospezione elettrica nella Val maggiore e zone limitrofe.

Coello Coello, C.A., Pulido, G.T. & Lechuga, M.S., 2004. Handling multiple objectives with particle swarm optimization, *IEEE Trans. Evol. Comput.,* **8**(3), 256–279.

Coello Coello, C.A., Lamont, G.B. & Veldhuizen, D.A.V., 2007. *Evolutionary Algorithms for Solving Multi-objective Problems,* 2nd edn, pp. 800, Springer.

Commer, M. & Newman, G.A., 2009. Three-dimensional controlled-source electromagnetic and magnetotelluric joint inversion, *Geophys. J. Int.,* **178**(3), 1305–1316.

Constable, S.C., Parker, R.L. & Constable, C.G., 1987. Occam's inversion: a practical algorithm for generating smooth models from electromagnetic sounding data, *Geophysics,* **52**(3), 289–300.

Dal Moro, G., 2010. Insights on surface wave dispersion and HVSR: joint analysis via Pareto optimality, *J. Appl. Geophys.,* **72**(2), 129–140.

Dal Moro, G. & Pipan, M., 2007. Joint inversion of surface wave dispersion curves and reflection travel times via multi-objective evolutionary algorithms, *J. Appl. Geophys.,* **61,** 56–81.

Deb, K. & Jain, H., 2014. An evolutionary many-objective optimization algorithm using reference-point-based nondominated sorting approach, part I: solving problems with box constraints, *IEEE Trans. Evol. Comput.,* **18**(4), 577–601.

Deb, K., Pratap, A., Agarwal, S. & Meyarivan, T., 2002. A fast and elitist multiobjective genetic algorithm, *IEEE Trans. Evol. Comput.,* **6,** 182–197.

De Luca, D.A., Destefanis, E., Forno, M.G., Lasagna, M. & Masciocco, L., 2014. The genesis and the hydrogeological features of the Turin Po Plain fontanili, typical lowland springs in Northern Italy, *Bull. Eng. Geol. Environ.,* **73**(2), 409–427.

De Luca, D.A., Comina, C., Lasagna, M., Destefanis, E., Masciocco, L., Godio, A. & Stocco, S., 2018. Effectiveness of geophysical surveys for water wells relocation in overexploited aquifers (the example of Maggiore and Traversola Valleys, northwestern Italy), *Environ. Earth Sci.,* **77,** 19, doi:10.1007/s12665-017-7218-0.

Edgeworth, F.Y., 1881. *Mathematical Physics,* P. Keagan.

Ekinci, Y.L. & Demirci, A., 2008. A damped least-squares inversion program for the interpretation of Schlumberger sounding curves. *J. Appl. Sci.,* **8,** 4070–4078.

Emami Niri, M. & Lumley, D.E., 2015. Simultaneous optimization of multiple objective functions for reservoir modeling, *Geophysics,* **80**(5), M53–M67.

Engelbrecht, A.P., 2007. *Computational Intelligence: An Introduction,* John Wiley & Sons Ltd.

Farquharson, C.G. & Oldenburg, D.W., 2004. A comparison of automatic techniques for estimating the regularization parameter in non-linear inverse problems, *Geophys. J. Int.,* **156**(3), 411–425.

Fernandez Martinez, J.L., Garcia Gonzalo, E., Fernandez Alvarez, J.P., Kuzma, H.A. & Menendez Perez, C.O., 2010. PSO: a powerful algorithm to solve geophysical inverse problems, *J. Appl. Geophys.,* **71**(1), 13–25.

Gallardo, L.A. & Meju, M.A., 2003. Characterization of heterogeneous near-surface materials by joint 2D inversion of dc resistivity and seismic data, *Geophys. Res. Lett.,* **30**(13), 1658, doi:10.1029/2003GL017370.

Godio, A. & Santilano, A., 2018. On the optimization of electromagnetic geophysical data: application of the PSO algorithm, *J. Appl. Geophys.,* **148,** 163–174.

Hering, A., Misiek, R., Gyulai, A., Ormos, T., Dobroka, M. & Dresen, L., 1995. A joint inversion algorithm to process geoelectric and sutface wave seismic data. Part I: basic ideas, *Geophys. Prospect.,* **43**(2), 135–156.

Ingeman-Nielsen, T. & Baumgartner, F., 2006. CR1Dmod: a matlab program to model 1D complex resistivity effects in electrical and electromagnetic surveys, *Comput. Geosci.,* **32,** 1411–1419.

Kennedy, J. & Eberhart, R., 1995. Particle Swarm Optimization, in *Proceedings of IEEE International Conference on Neural Networks IV,* Perth, WA, Australia, Vol. 1000, pp. 1942–1948.

Kennedy, J. & Eberhart, R., 2001. *Swarm Intelligence,* Morgan Kaufmann Publishers.

Lasagna, M., Caviglia, C. & De Luca, D.A., 2014. Simulation modeling for groundwater safety in an overexploitation situation: the Maggiore Valley context (Piedmont, Italy), *Bull. Eng. Geol. Environ.,* **73,** 341–355.

McNeill, J.D., 1990. Use of electromagnetic methods for groundwater studies, in *Geotechnical and Environmental Geophysics,* Vol. 1, pp. 191–218, ed. Ward, S.H., Society of Exploration Geophysicists.

Meju, M.A., 2005. Simple relative space–time scaling of electrical and electromagnetic depth sounding arrays: implications for electrical static shift removal and joint DC-TEM data inversion with the most-squares criterion, *Geophys. Prospect.,* **53,** 463–479.

Meqbel, N. & Ritter, O., 2015. Joint 3D inversion of multiple electromagnetic datasets, *Geophys. Prospect.,* **63,** 1450–1467.

Moorkamp, M., Jones, A.G. & Fishwick, S., 2010. Joint inversion of receiver functions, surface wave dispersion, and magnetotelluric data, *J. geophys. Res.,* doi:10.1029/2009JB006369.

Moorkamp, M., Heincke, B., Jegen, M., Roberts, A.W. & Hobbs, R.W., 2011. A framework for 3-D joint inversion of MT, gravity and seismic refraction data, *Geophys. J. Int.,* **184,** 477–493.

Musil, M., Maurer, H.R. & Green, A.G., 2003. Discrete tomography and joint inversion for loosely connected or unconnected physical properties: application to crosshole seismic and georadar data sets, *Geophys. J. Int.,* **153**(2), 389–402.

Paasche, H. & Tronicke, L., 2014. Nonlinear joint inversion of tomographic data using swarm intelligence, *Geophysics,* **79**(4), R133–R149.

Pace, F., Santilano, A. & Godio, A., 2017, Particle swarm optimization of electromagnetic data with parallel computing in the 2D case, in *Proceedings of 23rd European Meeting of Environmental and Engineering Geophysics,* Malmo, Sweden, doi:10.3997/2214-4609.201702021.

Pace, F., Santilano, A. & Godio, A., 2018. Multi-objective particle swarm optimization of vertical electrical sounding and time-domain electromagnetic data, in *Proceedings of 24th European Meeting of Environmental and Engineering Geophysics,* Porto, doi:10.3997/2214-4609.201802624.

Pace, F., Santilano, A. & Godio, A., 2019. Particle swarm optimization of 2-D magnetotelluric data, *Geophysics,* **84**(3), E125–E141.

Pallero, J.L.G., Fernández-Muñiz, M.Z., Cernea, A., Álvarez-Machancoses, O., Pedruelo-González, L.M., Bonvalot, S. & Fernández-Martínez, J.S., 2018. Particle swarm optimization and uncertainty assessment in inverse problems, *Entropy,* **20**(96), doi:10.3390/e20020096.

Pareto, V., 1896. *Cours d'Economie Politique,* Vols. I and II, F. Rouge.

Perez, R.E. & Behdinan, K., 2007. Particle swarm approach for structural design optimization. *Comput. Struct.,* **85,** 1579–1588.

Piatti, C., Boiero, D., Godio, A. & Socco, L.V., 2010. Improved Monte Carlo 1D inversion of vertical electrical sounding and time-domain electromagnetic data, *Near Surf. Geophys.,* **8,** 117–133.

Poli, R., 2008. Analysis of the publications on the applications of particle swarm optimisation, *J. Artif. Evol. Appl.,* **2008,** doi:10.1155/2008/685175.

Ratnaweera, A., Halgamuge, S.K. & Watson, H.C., 2004. Self-organizing hierarchical particle swarm optimizer with time-varying acceleration coefficients, *IEEE Trans. Evol. Comput.,* **8**(3), 240–255.

Reyes-Sierra, M. & Coello Coello, C.A., 2006. Multi-objective particle swarm optimizers: a survey of the state-of the-art, *Int. J. Comput. Intell. Res.,* **2**(3), 287–308.

Santilano, A., Godio, A. & Manzella, A., 2018. Particle swarm optimization for simultaneous analysis of magnetotelluric (MT) and time domain EM (TDEM) data, *Geophysics,* **83**(3), E151–E159.

Schnaidt, S., Conway, D., Krieger, L. & Heinson, G., 2018. Pareto-optimal multi-objective inversion of geophysical data, *Pure appl. Geophys.,* doi:10.1007/s00024-018-1784-2.

Sen, P.K., 1968. Estimates of the regression coefficient based on Kendall's tau, *J. Am. Stat. Assoc.,* **63**(324), 1379–1389.

Shaw, R. & Srivastava, S., 2007. Particle swarm optimization: a new tool to invert geophysical data, *Geophysics,***72**(2), F75–F83.

Shi, Y. & Eberhart, R.C., 1999. Empirical study of particle swarm optimization, in *Proceedings of the 1999 Congress on Evolutionary Computation, CEC 1999,* Washington, DC, USA, pp. 1945–1950.

Tarantola, A., 2005, *Inverse Problem Theory and Methods for Model Parameter Estimation,* Vol. 89, SIAM.

Theil, H., Amsterdam, Netherlands, 1950. A rank-invariant method of linear and polynomial regression analysis, in *Proceedings of the Royal Netherlands Academy of Sciences,* Vol. 53, parts 1, 2, 3.

Tripathi, P.K., Bandyopadhyay, S. & Pal, S.K., 2007. Multi-objective particle swarm optimization with time variant inertia and acceleration coefficients, *Inf. Sci.,* **177,** 5033–5049.

Tronicke, J., Paasche, H. & Böniger, U., 2011. Joint global inversion of GPR and P-wave seismic traveltimes using particle swarm optimization, in *6th International Workshop on Advanced Ground Penetrating Radar (IWAGPR),* Aachen, Germany, pp. 1–4.

Vozoff, K. & Jupp, D.L., 1975. Joint inversion of geophysical data, *Geophys. J. R. astr. Soc.,* **42,** 977–991.

Yang, C.H. & Tong, L.T., 1988. Joint inversion of DC, TEM, and MT data, in *58th Annual International Meeting,* pp. 408–410.

Key words

Authors are requested to choose key words from the list below to describe their work. The key words will be printed underneath the summary and are useful for readers and researchers. Key words should be separated by a semi-colon and listed in the order that they appear in this list. An article should contain no more than six key words.

COMPOSITION and PHYSICAL PROPERTIES
Composition and structure of the continental crust
Composition and structure of the core
Composition and structure of the mantle
Composition and structure of the oceanic crust
Composition of the planets
Creep and deformation
Defects
Elasticity and anelasticity
Electrical properties
Equations of state
Fault zone rheology
Fracture and flow
Friction
High-pressure behaviour
Magnetic properties
Microstructure
Permeability and porosity
Phase transitions
Plasticity, diffusion, and creep

GENERAL SUBJECTS
Core
Gas and hydrate systems
Geomechanics
Geomorphology
Glaciology
Heat flow
Hydrogeophysics
Hydrology
Hydrothermal systems
Infrasound
Instrumental noise
Ionosphere/atmosphere interactions
Ionosphere/magnetosphere interactions
Mantle processes
Ocean drilling
Structure of the Earth
Thermochronology
Tsunamis
Ultra-high pressure metamorphism
Ultra-high temperature metamorphism

GEODESY and GRAVITY
Acoustic-gravity waves
Earth rotation variations
Geodetic instrumentation
Geopotential theory
Global change from geodesy
Gravity anomalies and Earth structure
Loading of the Earth
Lunar and planetary geodesy and gravity
Plate motions
Radar interferometry
Reference systems
Satellite geodesy
Satellite gravity
Sea level change
Seismic cycle
Space geodetic surveys
Tides and planetary waves
Time variable gravity
Transient deformation

GEOGRAPHIC LOCATION
Africa
Antarctica
Arctic region
Asia
Atlantic Ocean
Australia
Europe
Indian Ocean
Japan
New Zealand
North America
Pacific Ocean
South America

GEOMAGNETISM and ELECTROMAGNETISM
Archaeomagnetism
Biogenic magnetic minerals
Controlled source electromagnetics (CSEM)
Dynamo: theories and simulations
Electrical anisotropy
Electrical resistivity tomography (ERT)
Electromagnetic theory
Environmental magnetism
Geomagnetic excursions
Geomagnetic induction
Ground penetrating radar
Magnetic anomalies: modelling and interpretation
Magnetic fabrics and anisotropy
Magnetic field variations through time
Magnetic mineralogy and petrology
Magnetostratigraphy
Magnetotellurics
Marine electromagnetics
Marine magnetics and palaeomagnetics
Non-linear electromagnetics
Palaeointensity
Palaeomagnetic secular variation
Palaeomagnetism
Rapid time variations
Remagnetization
Reversals: process, time scale, magnetostratigraphy
Rock and mineral magnetism
Satellite magnetics

GEOPHYSICAL METHODS
Downhole methods
Fourier analysis
Fractals and multifractals
Image processing
Instability analysis
Interferometry
Inverse theory
Joint inversion
Neural networks, fuzzy logic
Non-linear differential equations
Numerical approximations and analysis
Numerical modelling
Numerical solutions
Persistence, memory, correlations, clustering
Probabilistic forecasting
Probability distributions
Self-organization
Spatial analysis
Statistical methods
Thermobarometry
Time-series analysis
Tomography
Waveform inversion
Wavelet transform

PLANETS
Planetary interiors
Planetary volcanism

SEISMOLOGY
Acoustic properties
Body waves
Coda waves
Computational seismology
Controlled source seismology
Crustal imaging
Earthquake dynamics
Earthquake early warning
Earthquake ground motions
Earthquake hazards
Earthquake interaction, forecasting, and prediction
Earthquake monitoring and test-ban treaty verification
Earthquake source observations
Guided waves
Induced seismicity
Interface waves
Palaeoseismology
Rheology and friction of fault zones
Rotational seismology
Seismic anisotropy
Seismic attenuation
Seismic instruments
Seismic interferometry
Seismicity and tectonics
Seismic noise
Seismic tomography
Site effects
Statistical seismology
Surface waves and free oscillations
Theoretical seismology

Tsunami warning
Volcano seismology
Wave propagation
Wave scattering and diffraction

TECTONOPHYSICS
Backarc basin processes
Continental margins: convergent
Continental margins: divergent
Continental margins: transform
Continental neotectonics
Continental tectonics: compressional
Continental tectonics: extensional
Continental tectonics: strike-slip and transform
Cratons
Crustal structure
Diapirism
Dynamics: convection currents, and mantle plumes
Dynamics: gravity and tectonics
Dynamics: seismotectonics
Dynamics and mechanics of faulting
Dynamics of lithosphere and mantle
Folds and folding
Fractures, faults, and high strain deformation zones
Heat generation and transport
Hotspots
Impact phenomena
Intra-plate processes
Kinematics of crustal and mantle deformation
Large igneous provinces
Lithospheric flexure
Mechanics, theory, and modelling
Microstructures
Mid-ocean ridge processes
Neotectonics
Obduction tectonics
Oceanic hotspots and intraplate volcanism
Oceanic plateaus and microcontinents
Oceanic transform and fracture zone processes
Paleoseismology
Planetary tectonics
Rheology: crust and lithosphere
Rheology: mantle
Rheology and friction of fault zones
Sedimentary basin processes
Subduction zone processes
Submarine landslides
Submarine tectonics and volcanism
Tectonics and climatic interactions
Tectonics and landscape evolution
Transform faults
Volcanic arc processes

VOLCANOLOGY
Atmospheric effects (volcano)
Calderas
Effusive volcanism
Eruption mechanisms and flow emplacement
Experimental volcanism
Explosive volcanism
Lava rheology and morphology
Magma chamber processes
Magma genesis and partial melting
Magma migration and fragmentation
Mud volcanism
Physics and chemistry of magma bodies
Physics of magma and magma bodies
Planetary volcanism
Pluton emplacement
Remote sensing of volcanoes
Subaqueous volcanism
Tephrochronology
Volcanic gases
Volcanic hazards and risks
Volcaniclastic deposits
Volcano/climate interactions
Volcano monitoring
Volcano seismology